Feldspar alteration by disequilibrium CO_2-H_2O fluids in reservoir sandstones: Implications for CCS

Authors: Natalie. J.C. Farrell[1], Lining Yang[2], Michael. J. Flowerdew[3], Chris Mark[4], Buhari Ardo[1], Kevin. G. Taylor[1], Nico Bigaroni[1], Michael. Pointon[3], Lewis Hughes[1], John Waters[1], Lee Paul[1]

1. Department of Earth and Environmental Sciences, Williamson Building, University of Manchester, Manchester, United Kingdom
2. Institute of Marine Sciences (CNR-ISMAR), Bologna, Italy
3. CASP, Cambridge, United Kingdom
4. Department of Geology, Swedish Museum of Natural History, Stockholm, Sweden

*Corresponding author e-mail address: natalie.farrell@manchester.ac.uk. Co-author email addresses: li-ning.yang@outlook.com, michael.flowerdew@casp.org.uk, chris.mark@nrm.se, buhari.ardo@gmail.com, kevin.taylor@manchester.ac.uk, nico.bigaroni@manchester.ac.uk, michael.pointon@casp.org.uk, lewis.hughes@manchester.ac.uk, john.waters@manchester.ac.uk, lee.s.paul@manchester.ac.uk,

Keywords: Feldspar, CCS, Sandstone, reaction texture, dissolution, precipitation, calcite cement

Abstract [288/300]

Understanding how the minerals in reservoir rocks respond to CO_2 injection is vital for the success and safety of Carbon Capture and Storage (CCS) projects. Feldspars are the most common mineral in the Earth's crust and act as primary framework grains in sandstones. Compared to quartz, feldspars are mechanically weak and chemically reactive. Dissolved feldspars can re-precipitate as clays, which in CCS reservoirs could impact fluid-flow. While caprock mineral stability is well studied, reservoir mineral reactivity, particularly of feldspars, remains understudied. To address this knowledge gap, we present microstructural and geochemical data from batch experiments that reacted CO_2-enriched fluids with feldspar-bearing sandstone sampled from the Captain Sandstone Member, the primary reservoir for the Acorn CCS Project (UK).

Experiments were conducted in a hydrostatic pressure vessel at 70 MPa confining pressure, 50 MPa pore pressure, and temperatures ranging from 80°C to 550°C, using CO_2-enriched water to simulate reservoir conditions. Pre- and post-reaction samples were analysed using XRD,

SEM-EDS, and XCT to assess microstructural and mineralogical changes. Results show that CO_2:feldspar interactions differ significantly from control experiments involving water alone. At reservoir-relevant temperatures (80°C), incongruent dissolution of K-feldspar weakened grains which led to microfracturing. At 250°C, CO_2 fluids caused total dissolution of calcite grains and cement and selective leaching of calcium from oligoclase, enriching the pore fluid with Ca^{2+}. Above 400°C, coupled dissolution–precipitation processes were observed, including congruent K-feldspar dissolution, secondary porosity development, and localised precipitation of Ca-aluminosilicates and K-bearing phases around dissolving K-feldspars. These transformations could alter reservoir flow pathways and induce mechanical risks, i.e. destabilising nearby faults or initiating reservoir collapse. Given feldspars' prevalence in crustal rocks and CCS sandstone reservoirs, their reactive behaviour under in-situ conditions and in the presence of aggressive fluids demands greater attention.

1. Introduction

Carbon Capture and Storage (CCS) projects aim to moderate the impacts of climate changes by injecting supercritical CO_2 into porous rock, such as deep saline aquifers and depleted hydrocarbon sandstone reservoirs, where it is intended to be stored for 10,000 years/indefinitely (IPCC, 2005). The productivity and safety of CCS projects hinge on our ability to efficiently flow CO_2 fluids into subsurface rock formations while preventing leakage. A key challenge for success is the ability to predict dynamically changing fluid-flow during injection and CO_2 plume migration (Juanes et al, 2006; Benson and Cole, 2008; Ringrose, 2020). This requires both a specific knowledge of the pre-injection micro-scale reservoir properties, e.g., pore volume, pore connectivity, grain texture, and a broader empirical understanding of how injected fluids might mechanically and/or chemically alter this microstructure and thereby impact CCS project efficiency and safety (Rochelle et al, 2004; Hall et al, 2015; Rathnaweera et al, 2015; Shogenov et al, 2015; Fuchs et al, 2019; Foroutan et al, 2021; Pessu et al, 2025). Experimental studies have explored these CO_2-fluid-sandstone interactions showing that the acidic brines created by dissolution of CO_2 into formation fluids enhances dissolution of carbonate minerals, primarily as cements in sandstone reservoirs (Ross et al, 1982; Bertier et al, 2006; Hangx et al, 2013) with fewer studies reporting CO_2 fluid alteration of reactive aluminosilicates, including feldspars (Bertier et al, 2006; Hall et al, 2015; Lu et al. 2013). Geochemical models indicate that feldspar alteration may result in precipitation of carbonate minerals e.g., dolomite and dawsonite, which could permanently 'lock-in' CO_2

64 (Durst et al., 2000, Seisenbayev et al, 2023). Feldspar:CO_2 reactivity could substantially

65 influence the performance and stability of CCS reservoirs, yet their response to saturation with

66 CO_2-enriched fluids under reservoir conditions (temperature *and* stress), including reaction

67 types and rates and the consequences of reactivity, is poorly understood (Lu et al. 2013). This

68 is a key knowledge gap especially in polymineralic rocks like sandstone where coupled

69 chemical–mechanical processes are already poorly constrained.

70 *1.1.Feldspar solubility*

71 Feldspars are a volumetrically significant, mechanically weak and chemically reactive

72 framework mineral in sandstones (Tullis and Yund, 1977) and most crustal rocks. In

73 comparison to quartz, feldspars are highly reactive (Knauss and Wolery, 1986; Dove and

74 Crerar, 1990). They can dissolve creating significant secondary porosity (Farrell and Healy,

75 2017) and re-precipitate as clays, which impede fluid-flow and mechanically weaken rocks

76 (Farrell et al, 2021; Summers and Byerlee, 1977; Collettini et al, 2019 respectively), outcomes

77 that could compromise both CCS reservoir efficiency and mechanical integrity. Feldspar

78 solubility is strongly influenced by pH, as demonstrated in early experimental studies (Correns,

79 1961; Wollast, 1967). These investigations established that feldspar dissolution rates increase

80 significantly under acidic conditions due to enhanced hydrolysis of Si–O and Al–O bonds in

81 the crystal lattice, the rate of which is determined by grain surface area (Helgeson et al, 1984).

82 Feldspars are mineralogically well defined, but their subsurface behaviour is uncertain. As key

83 framework minerals in many of Earth's oldest crustal rocks e.g., gneisses, granites and

84 sandstones, they can preserve evidence of their extensive geological histories (e.g. weathering,

85 transport, burial, fluid interaction), which are reflected in their diverse microstructural textures

86 and chemical heterogeneity. This inherited heterogeneity directly affects their reactivity.

87 Across kilometre-scale reservoirs, their solubility can differ significantly based on provenance

88 (detrital sources) and their burial or fluid-flow history (Glasmann, 1992), making some grains

89 more or less prone to dissolution. Chemical alteration has been shown to enhance stress-

90 corrosion cracking in quartz (Scholz, 1972), hence deformation of more reactive feldspars (via

91 chemical dissolution and mechanical cracking) in the presence of chemically active CO_2 fluids

92 is expected.

93 *1.2.Predicting feldspar reaction rates*

94 Mineral reaction rates are typically defined by experiments on powdered rock samples

95 (Brantley et al, 2008). While using powders allows for control over reactant surface area, this

96   method fails to account for the grain-to-grain stresses present in subsurface rocks. Even in
97   hydrostatic experiments, such stresses at the grain scale can significantly accelerate mineral
98   dissolution rates, often exceeding predictions based on powder-derived rate laws (Rutter, 1976;
99   Wheeler, 1991). Considering the inherent weakness of feldspars under pressure-temperature
100   conditions in the shallow crust, these stresses could induce microfracturing, which increases
101   surface area and exposes fresh reactive surfaces that drive further reaction. Geochemical
102   simulations frequently oversimplify feldspars, disregarding their diverse chemical
103   compositions and variable textures i.e., surface areas, which are crucial for accurate reaction
104   rate predictions (Helgeson et al, 1984). Enhanced understanding of feldspars, from quantifying
105   the compositional variability in target reservoirs, to empirical evidence of feldspar:CO_2
106   reactions i.e., dissolution rates and secondary mineral formation, should improve the accuracy
107   of geochemical and reactive transport models. We hypothesise that injection of CO_2 enriched
108   fluids will impact the solubility of *stressed* feldspar grains and potentially alter the properties
109   of sandstone CCS reservoirs, specifically the pore volume, pore connectivity, permeability and
110   geomechanical stability.

111   This paper presents microstructural insights from a suite of coupled chemical:mechanical
112   reaction experiments on feldspar-bearing sandstones from the Early Cretaceous Captain
113   Sandstone Member from the Moray Firth, Scotland, the target reservoir for the Acorn CCS
114   Project (Alcalde et al, 2019), highlighting the impact of CO_2 fluid saturation on reactive
115   framework grains under subsurface conditions. In this study we used an externally heated,
116   hydrostatic pressure vessel to investigate the solubility of various feldspars in a CO_2 saturated
117   sandstone under hydrostatic stress, simulating CCS reservoir conditions in closed batch system
118   experiments. Experiments were conducted at a range of increasing temperatures, effectively
119   accelerating reaction rates simulating mineral reactions over hundreds of years – aligning with
120   the timescales required for CO_2 storage. The temperature dependence of mineral dissolution
121   follows an Arrhenius relationship, linking the reaction rate constant to temperature. For K-
122   feldspar, the baseline rate constant is well-established, and we approximate its temperature
123   dependency using established rate laws for dissolution in varying pH fluids (Helgeson, 1984;
124   Blum and Stillings, 1995). Unlike previous Captain Sandstone experimental studies that
125   focused solely on reservoir mechanical stability using water as a pore fluid at ambient
126   temperatures (Allen et al, 2020) or on the mechanical impact of CO_2 fluids on carbonate cement
127   dissolution at low temperatures in an open pore fluid system (Hangx, 2013), this research
128   explores the role of CO_2 fluid chemistry on the dissolution and stress-induced deformation of

129 arguably more important *framework* grains over geological timescales. These results address a
130 major knowledge gap in CCS reservoir appraisal and have scope to provide empirical
131 constraints for long-term CO_2 containment predictions.

132 **2. Material and Methods**

133 This study used an overlapping programme of experimental rock deformation, microstructural
134 and geochemical analysis to characterise the range/integrity of feldspars contained in a CCS
135 target sandstone samples in the context of the reservoir geological history; experimentally
136 assess how feldspars interact with CO_2-enriched fluids under subsurface conditions
137 (temperature, pressure and grain scale stress) and consider the effect of feldspar dissolution
138 and subsequent precipitation of clay minerals on reservoir properties of fluid-flow and
139 mechanical strength. The characterisation of pre-experiment, in situ Captain Sandstone
140 feldspars is summarised in Section 2.1 and reported along with a compositional analysis and a
141 provenance model for direct and recycled feldspars by Flowerdew et al., 2024.

142 *2.1. Material*

143 Core plugs used in these experiments were taken from two sites within the historic petroleum
144 well (14/29a-5, Goldeneye Field, around 8500 ft/2590.8 m), specifically from the D sand top
145 and D sand middle intervals. These sandstones form the target 'D sand' unit of the planned
146 CO_2 storage reservoir at the Acorn CO_2 storage site, Scotland (Alcalde et al., 2019). The
147 principal reservoir consists of fine to medium grained, high porosity, subarkosic turbidite
148 deposits (Pinnock et al, 2003; Stewart and Marshall, 2020). Detrital mineralogy is dominated
149 by quartz, plagioclase (albite and oligoclase) and orthoclase with some mica, glauconite and
150 mudclasts. Some feldspars in the 'D sand' subdivision of the Member have already been very
151 reactive as shown by secondary porosity (Stewart and Marshall, 2020), more prominent at its
152 top.

153 Captain Sandstone 'D sand' samples comprise poorly cemented subarkose (Folk et al, 1970).
154 Thin section analysis showed that grains are moderately to poorly sorted, 50 to >1000 μm in
155 diameter and loosely packed with around 30% pore area. Intergranular pores are large and
156 irregular or smaller and angular formed by the intersections of multiple rounded grains (Fig
157 1.a). X-ray diffraction analysis showed that samples broadly contain 76% quartz, 8%
158 plagioclase, 8% K-feldspar, 6% clays, predominantly kaolinite plus minor amounts of 1%
159 calcite, 1% glauconite (XRD method and results, Table 2, Supp. Mat,). Mineralogical makeup

160 was also determined by using element data obtained from scanning electron microscopy energy
161 dispersive X-ray spectroscopy (hereafter abbreviated to EDS) mapping overlain on
162 Backscattered electron images (BSE) taken using a Scanning Electron Microscope (SEM) (Fig
163 1.b).
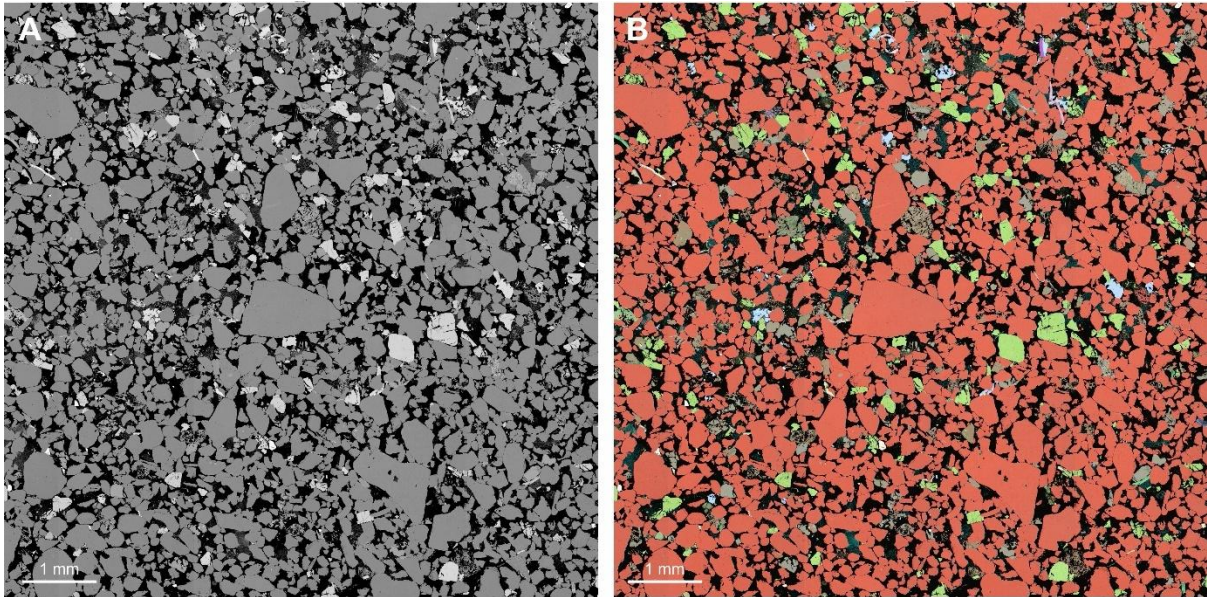
164
165 **Fig 1. Back scattered Electron and semi-transparent EDS elemental maps of pre-experiment D sand,**
166 **Captain Sandstone (a and b respectively). Black = pore/void space, red/orange = quartz, green/yellow =**
167 **orthoclase, grey/brown = oligoclase, pale blue = calcite**

168 Captain Sandstone feldspars are mineralogically and texturally diverse showing three dominant
169 mineralogies; two plagioclases, intermediate NaCa bearing oligoclase and end member Na-rich
170 albite and K-feldspar (Figure 2.a - e). The reactivity of plagioclase is already apparent in the
171 pre-experiment samples, as indicated by the skeletal texture of albite grains (Fig. 2.b). This
172 texture likely results from the albitisation of oligoclase, driven by chemical exchange where
173 Ca in oligoclase is replaced by Na from brines, substituting Ca^{2+} ions with Na^+, and releasing
174 Ca^{2+} into the fluid (Fig. 2.c). Additionally, plagioclase reaction and dissolution (whether
175 oligoclase or albite) has likely released Al and Si to form kaolinite precipitates during
176 geological diagenesis (Figs. 2.b and c). Both plagioclase and oligoclase grains commonly range
177 between ~100 – 200 µm diameters and display blocky, sub-rectangular grain boundaries with
178 rounded edges (Fig. 3, Supp. Mat,). K-feldspars tend to be larger than plagioclases, averaging
179 200-300 µm diameter and display coherent, rounded grain boundaries abutting similarly shaped
180 quartz grains (Fig 2.c). Many K-feldspars show perthite textures with darker fine bands and
181 streaks of albite lamellae oriented along cleavage planes (Fig 2.d and Fig 3. Supp. Mat,). Some
182 K-feldspars show reaction in perthite grains with some preferential dissolution of albite
183 lamellae and opening up of intergranular porosity along these features (Fig. 2.f).
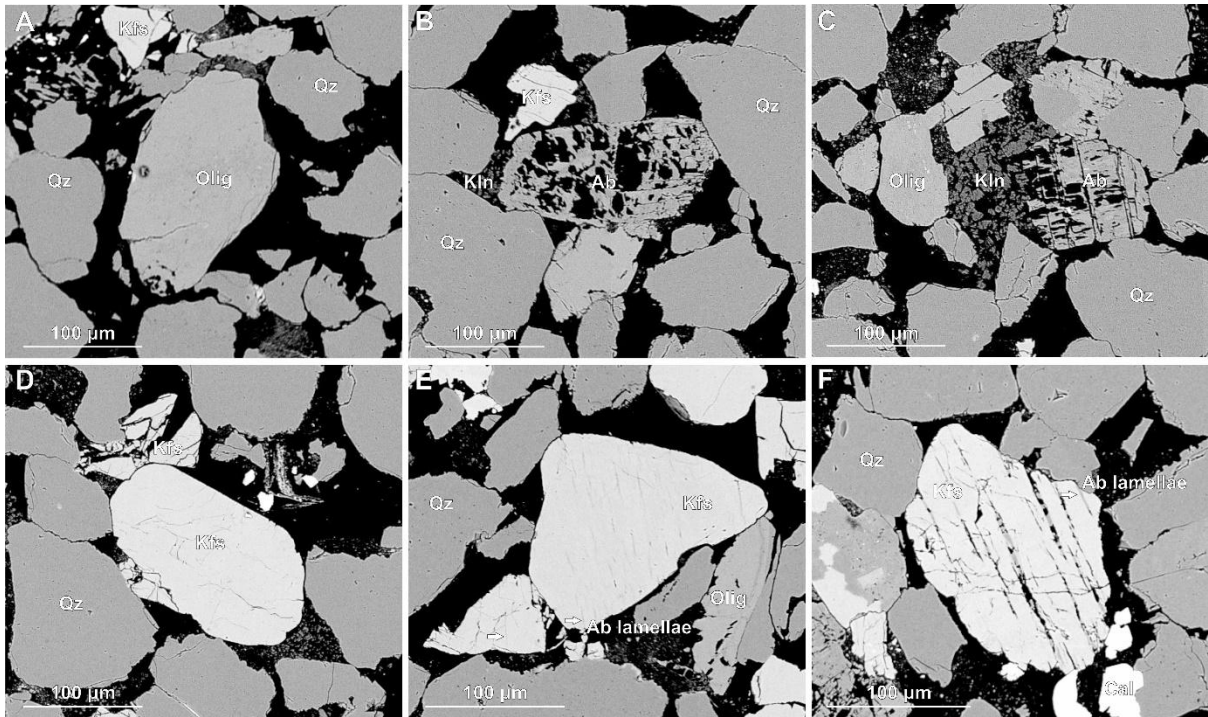
Figure 2. Back Scattered Electron images showing feldspar types including plagioclases, oligoclase (a and c) and albite (b and c) and K- feldspar (d-f) in pre-experiment samples of Captain Sandstone. Abbreviations follow Whitney and Evans, 2010. Quartz (Qz), (Oligoclase (Olig), K-feldspar (Kfs), Albite (Ab), Kaolinite (Kln).

2.2. Experimental method

Eight reaction experiments were performed on 9.5 mm diameter core plugs of Captain Sandstone Member 'D sand' using hydrostatic pressure vessels at ~70 MPa confining pressure (Pc) aka ~3 km burial depth with 50 MPa pore fluid pressure (Pf). Four experiments used CO_2 saturated water as a pore fluid (as a proxy for CO_2 injection), while four control experiments used H_2O under the same conditions. We experimentally modelled the progression of feldspar reactivity under subsurface conditions by conducting experiments across a range of temperatures (from 80°C, aka reservoir conditions, up to 550°C), using elevated temperatures as a proxy for longer reaction time. This approach uses the Arrhenius equation, which describes the temperature dependence of reaction rates, allowing higher temperatures to accelerate mineral reactions and simulate longer-term geochemical processes within practical and repeatable laboratory timescales (calculated reaction rate ratios for these experiments detailed in Supp. Mat.). These results can then be extrapolated to reservoir temperatures following standard practice in mineral-reaction studies (Blum and Stillings, 1995), a methodology commonly used to model reservoir evolution over geological timescales (Brantley et al, 2008; Hangx and Spiers, 2009; Hellmann et al., 2012). Experimental conditions are detailed in Table 1.

Sample ID	Rig ID	Pore Fluid Chemistry	Temperature (°C)	Confining Pressure (MPa)	Pore Fluid Pressure (MPa)	Duration (days)
Dt02	Nimonic 3	H_2CO_3	80	70	50	6
Dm07	Nimonic 2	H_2O	80	70	50	6
Dt01	Nimonic 3	H_2CO_3	250	70	50	10
Dm04	Nimonic 2	H_2O	250	77	50	10
Dt03	Nimonic 3	H_2CO_3	400	70	50	6
Dm06	Nimonic 2	H_2O	400	75	50	6
Dm01	Nimonic 3	H_2O	550	72	50	6
Dm05	Nimonic 3	H_2CO_3	550	80	50	6

Table 1. Experimental conditions for batch reactor tests conducted in triaxial deformation rigs 'Nimonic 2' and 'Nimonic 3'. Core plugs of Captain Sandstone were reacted with differing pore fluid chemistries under constant Pf, Pc and temperatures for durations of 6-10 days with the objective of assessing the influence of pore fluid chemistry and temperature on mineral stability and microstructure.

Experiments were conducted using externally heated triaxial deformation apparatus, 'Nimonic 2' and 'Nimonic 3'. The pressure vessel and sample assembly in these rigs are constructed from nickel alloy (Nimonic® 115) which is highly resistance to oxidation and compatible with carbonic acid and other corrosive fluids at elevated temperatures, preventing piston reactions that could contaminate the rock sample (Fig 3). Samples were contained within annealed copper jackets to isolate them from the water confining fluid, which was pressurised to reservoir conditions using a compressed air pump. Both Pc and Pf were gradually increased in succession up to the required experiment conditions to prevent pore collapse and preserve the starting material grains and microstructure. For control experiments, the pore fluid was tap water (very soft with total hardness of 16 mg/L, Supp. Mat, Table 1), while for CO_2 proxy experiments, the same water was saturated with CO_2 using a SodaStream®. The resulting 'fizzy water' contained ~6 g/L CO_2, yielding a pH of 4. Pf was controlled using a pore volumometer with a piston driven by a DC servo-motor. This system allowed precise adjustments of the piston in and out of a 3 cm³ pressure vessel to maintain a constant Pf through feedback control from a pore pressure transducer. A 50 MPa Pf was used in all experiments to ensure that water remained in a liquid state even above its critical point ~400°C, thereby preserving consistent stress conditions throughout the experiments. Once at pressure, the experiment temperature was applied using upper and lower external furnaces which create a thermal gradient which can be used to position a 'hot spot' within the pressure vessel focused around the relatively small sample. The furnace temperature was increased to the required level using variacs, which control the voltage to the furnaces for precise adjustments. The temperature was then maintained at the set value for six days with stable power regulation from the variacs. Sample temperature was monitored using an inconel-sheathed thermocouple inserted down the upper

234 piston. Pre experiment calibrations showed a temperature range of <2°C along the sample

235 length at 500°C. Experiments were ended by decreasing temperature back to ambient

236 conditions then unloading the Pf and Pc in tandem and in reverse to protect the pore space.
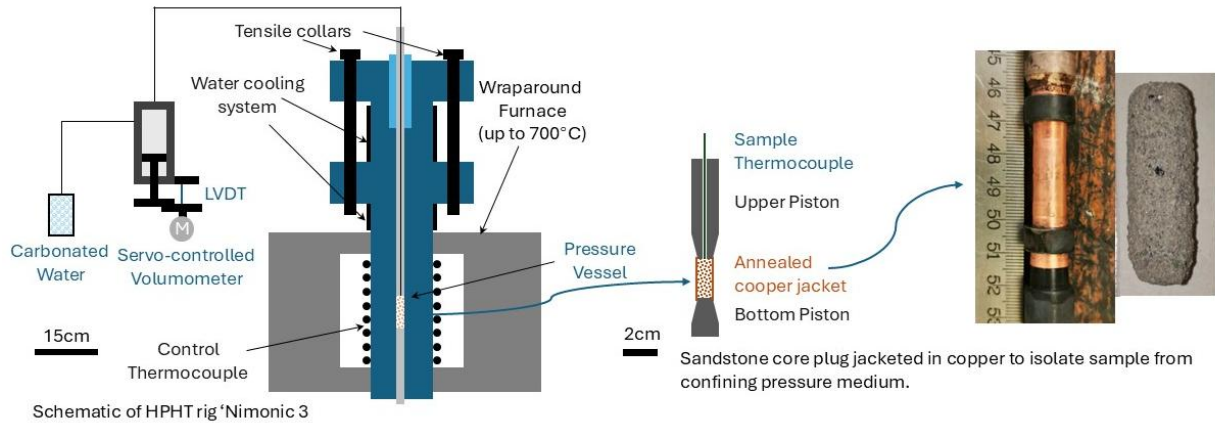
237
238 **Figure 3. Schematic cross section diagram of high pressure, high temperature triaxial rig 'Nimonic 3'**
239 **illustrating the sample assembly within the Nimonic pistons (rhs), confinement of sample with the pressure**
240 **vessel and furnace (centre) and pore volumometer controlling injection and pressure of pore fluid along**
241 **the top piston (lhs).**
242

243 *2.3. Microstructural analysis*

244 Post experiment jacketed core plugs were injected with epoxy under a vacuum and then halved

245 to make thin sections covering the central portion of the sample cylinder. Polished sections

246 were carbon coated before being imaged using a Zeiss Evo MA 15 scanning electron

247 microscope housed at CASP. Back scattered electron (BSE) images and elemental maps were

248 collected using one or a combination of a Zeiss Back Scatter Electron (BSE) detector, an

249 Oxford Instruments Ultim Max 100 Energy dispersive x-ray spectrometer (EDS) detector and

250 an Oxford Instruments Unity detector. Montages of images that cover the thin section were

251 collected at 20 kV and 2000 pA probe current, and 10 kV and 200 pA probe current where

252 greater definition imagery was required. Images and data were collected, manipulated and

253 exported using Oxford Instruments AZtec software version 6.1, coupled with the

254 AutoPhaseMap and AZtecFeature analysis and CASP's in-house mineral classification

255 scheme.

256 Microstructural analysis was conducted on BSE and EDS images of pre- and post-experiment

257 thin sections to examine and characterise mineral phases and textures and analyse reaction

258 pathways between grains. This analysis was facilitated by the generation of EDS x-ray spectra

259 for specific points or regions on the map. Post experimental mineral dissolution and/or

260 precipitation was quantified from BSE maps overlain with semi-transparent EDS maps by

261 thresholding the area covered by key mineral phases (K-feldspar, plagioclase, calcite) using

262 image analysis software ImageJ and defining this result as a percentage of the total grain

263 content (see Section 1.4, Supp. Mat, for more information). Individual montage images were

264 analysed separately to investigate the heterogeneity of pore and grain distributions (as per

265 method in Farrell and Healy, 2017). Additional 3D micro-CT images were produced of pre and

266 post experiment samples to assess grain deformation and pore networks. The micro-CT data

267 had limited resolution compared to the SEM data and so are not discussed here but are included

268 in the Supplementary Materials.

269 **3. Results**

270 Microstructural and compositional changes were identified in all experimentally reacted

271 samples indicating cation exchange between pore fluid and sandstone samples after

272 experimental run times of six days. The experimental duration, stress conditions and pore fluid

273 compositions are summarised in Table 1. In this section we present petrographic results for

274 specific mineral phases and their alteration in the presence of CO_2-enriched water compared

275 with H_2O (i.e. tap water) (Fig 4-10). Image analysis was used to quantify the extent of mineral

276 alteration in post-experiment samples compared to pre-experiment. Mineral quantifications are

277 presented as box plots to show changes in mean mineral content which could be used in

278 geochemical models and to illustrate the statistical distribution and variability of mineral grains

279 within samples, highlighting dissolution heterogeneity (Fig 11). Additional microstructural

280 data from all experiments are shared in a Supplementary Materials document (Supp. Mat.).

281 *3.1. Alteration of K-feldspar*

282 *3.1.1. K-feldspar:CO_2 enriched pore fluids*

283 Post-experiment BSE imaging reveals significant microstructural changes in K-feldspar grains

284 reacted at different temperatures. Compared to pre-experiment samples, which exhibit minimal

285 fracturing (Fig. 2.d-f, and Supp. Mat. Fig. 3), post-experiment K-feldspar grains display

286 dissolution, systematic microfracturing and grain fragmentation and development of secondary

287 porosity providing evidence of active mineral alteration during experiments (Fig. 4; Supp. Mat.

288 Figs. 5–8).

289 At 80°C, open pores develop on grain surfaces as linear and parallel 'cracks' or 'seams' that

290 propagate into grain interiors at high angles, often forming bimodal cross-cutting sets aligned

291 with cleavage planes (Fig. 4.a–b; Supp. Mat. Figs. 5–6) and commonly oriented with albitised

lamellae (Fig. 5.a). Some tightly packed K-feldspars are fractured against adjacent grains and crushed between quartz grains, which remain largely intact, suggesting mechanical weakening of stressed K-feldspars, likely enhanced by localised dissolution and development of porous 'seams' on the grain edges (Supp. Mat. Fig. 5). At 250°C intergranular dissolution becomes more pronounced, suggesting that increased intergranular fracture density both enhanced reactive surface area and created conduits for further fluid-rock interaction (Fig. 4.c). At 400°C, K-feldspar dissolution is accompanied by the formation of thin (~3 μm), discontinuous calcic aluminosilicate overgrowths along open grain boundaries, particularly around smaller K-feldspar fragments (Fig. 4.d; Fig. 5.b). EDS spot analysis shows overgrowths are chemically equivalent to calcic plagioclase (andesine- anorthite) (Supp Mat. Fig 17). At 550°C, intergranular fractures widen (5–10 μm vs. <5 μm at 400°C), and K-feldspars are segmented by cross-cutting fractures into fragments with rounded, dissolution-modified edges (Fig. 4.e–f). In this sample secondary porosity is widespread and these pores can often be identified by "ghosts" of former grain outlines defined by secondary clay precipitates (Supp. Mat. Figs. 6–8 and XCT images and animations, https://doi.org/10.6084/m9.figshare.30061294.v1).
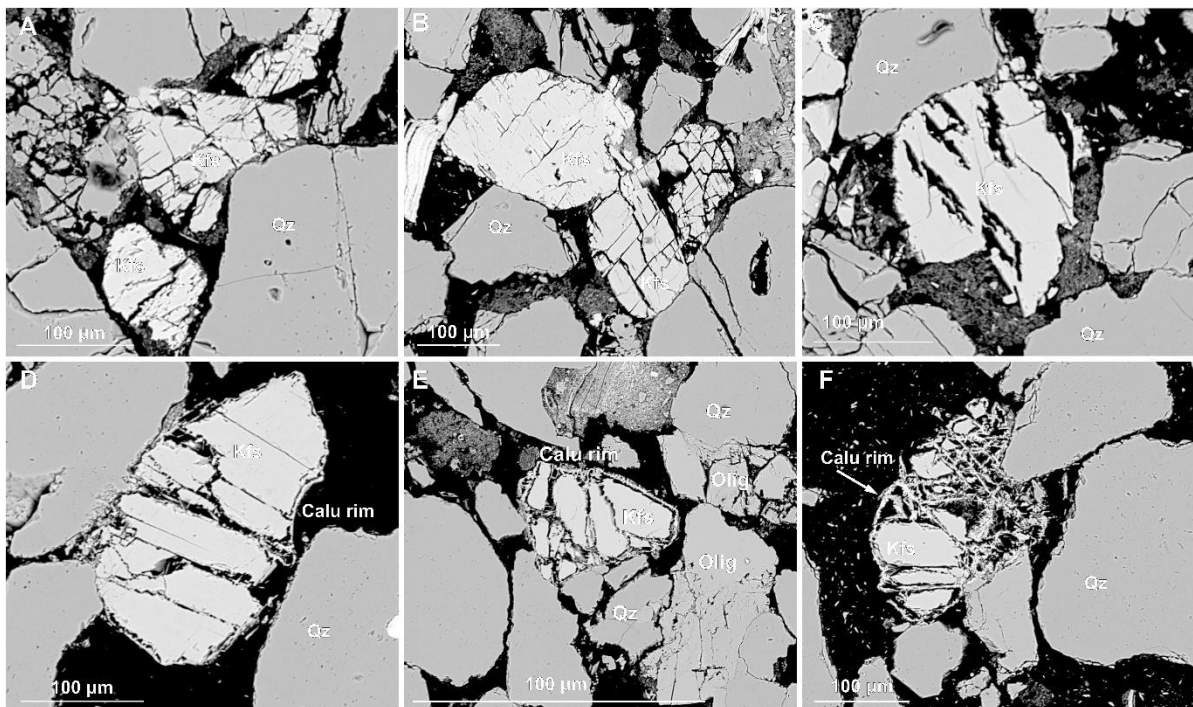
Figure 4. Back scattered electron (BSE) images showing progressive K-feldspar (Kfs) alteration via chemical and mechanical deformation with increasing temperature reaction experiments conducted with CO₂ fluids at hydrostatic conditions, including – dissolution and grain microfracturing at experiments conducted at 80°C (a and b), grain dissolution at 250°C (c), and secondary mineral growth around K-feldspar grains at 550°C (d - f). Quartz (Qz), (Oligoclase (Olig), K-feldspar (Kfs), Calcic aluminosilicate (Calu).

314 Secondary precipitation phases are most prominent at higher temperatures (400–550 °C),
315 appearing as a Ca-rich pale blue and K-rich bright green phases in combined EDS-BSE images
316 (Fig. 5). Precipitates are often located around 'free' edges of grains i.e. not in contact with
317 adjacent grains and become thicker (~10 μm) and more continuous at 550°C, while grain to
318 grain boundaries display concave-convex contacts with adjacent quartz grains, implying
319 differential dissolution and possible influence of intragranular stress on reactivity (Fig. 5.c).
320 Dissolved K-feldspar grain edges typically exhibit irregular, serrated morphologies (Fig. 5.d;
321 Supp. Mat. Figs. 7–8). In some images, a narrow void separates receding K-feldspar grain
322 edges from calcitic overgrowths, marking a zone where dissolution likely outpaced
323 precipitation (Fig. 4.d–f; Fig. 5.c–d). High-magnification imaging shows outward nucleation
324 of these calcic aluminosilicates at high angles from K-feldspar surfaces and aligned
325 crystallographically with the host grain (Fig. 5.d). Thin K-feldspar strands remain linked to the
326 overgrowths, suggesting ongoing elemental exchange. A K-rich phase, likely mica, is also
327 observed as a bright green band within and beyond the pale blue rims, forming spindly, fibrous
328 morphologies (Fig. 5.d). In the high temperature experiments, the K-rich phase is also
329 precipitated in pore space and pore throats, within the clay masses small crystals of the calcic
330 aluminosilicate has nucleated (Fig. 5.b).
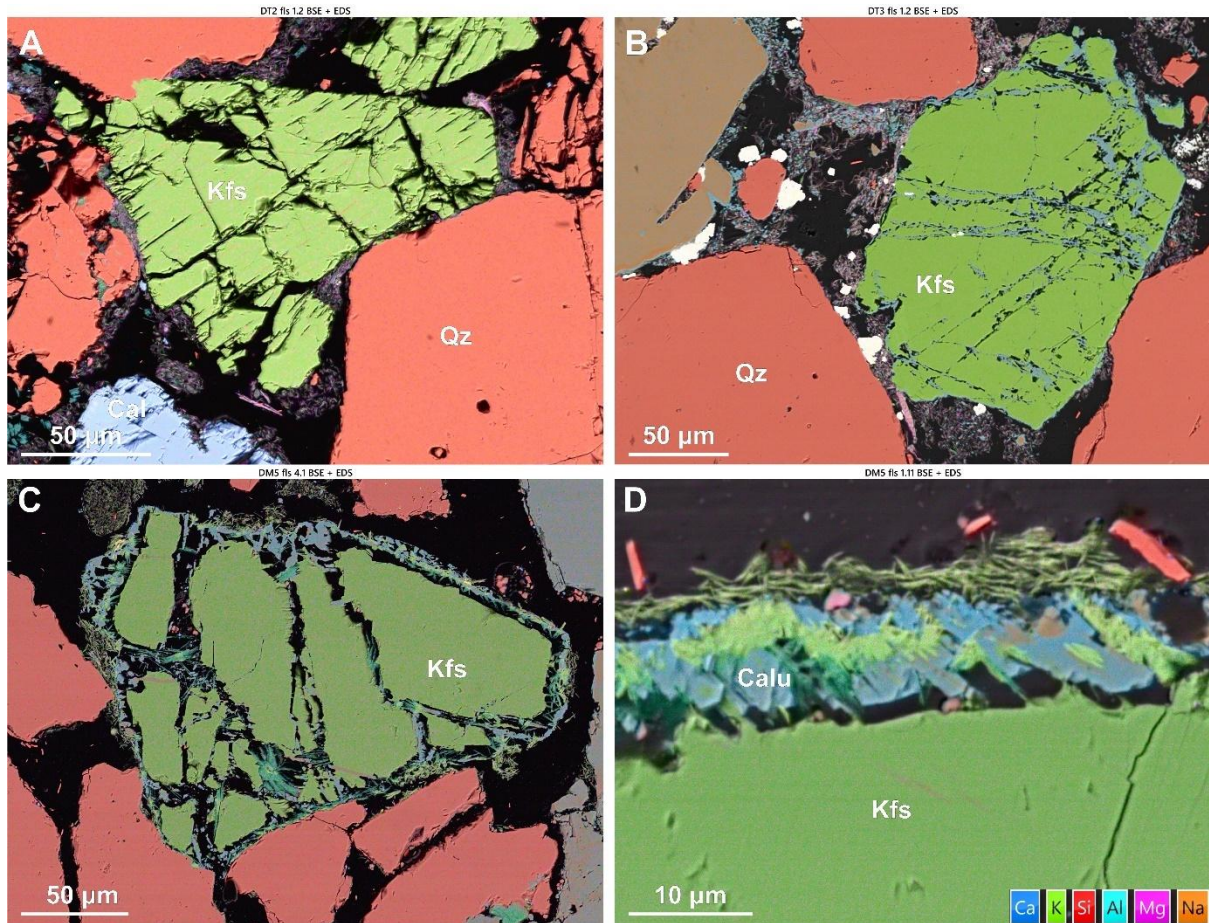
Figure 5. High-magnification backscattered electron (BSE) images, overlaid with semi-transparent elemental EDS maps, showing progressively enhanced microfracturing, dissolution, and secondary precipitation in K-feldspar saturated with CO2 enriched fluids at a range of experimental temperatures (80°C (a), 400°C (b), and 550°C (c, d).

3.1.2. K-feldspar:H_2O pore fluids

In H2O experiments (tap water as pore fluid), post-reaction samples show temperature-dependent microstructural changes distinct from those observed under CO_2-enriched fluid conditions. At 80°C, microfractures in K-feldspar are primarily grain-bound, with curvilinear to sub-parallel orientations (Fig. 6.c–d), the latter suggesting crystallographic control and possible mechanical weakening. These features differ from the chemically driven dissolution seams, serrated grain edges, and widening of intragranular fractures observed in the CO_2 experiments (Section 3.1.1). At higher temperatures 400°C, K-feldspars appear to have been mechanically weakened with post experiment samples showing enhanced intergranular fracturing, local grain crushing, and some convex–concave grain contacts. At 550°C, K-feldspars in H_2O experiments exhibited irregular intergranular fracturing and precipitation of calcic aluminosilicate overgrowths and a K-rich phase which also formed discontinuous rims around grain edges (Fig. 6; Supp. Mat. Figs. 9–12). However, unlike the CO_2 experiments, these rims are thinner and more spatially limited, and K-feldspar dissolution features were less

13

pronounced. These contrasts highlight the influence of pore fluid chemistry on K-feldspar enhanced reactivity under CO_2-enriched conditions.
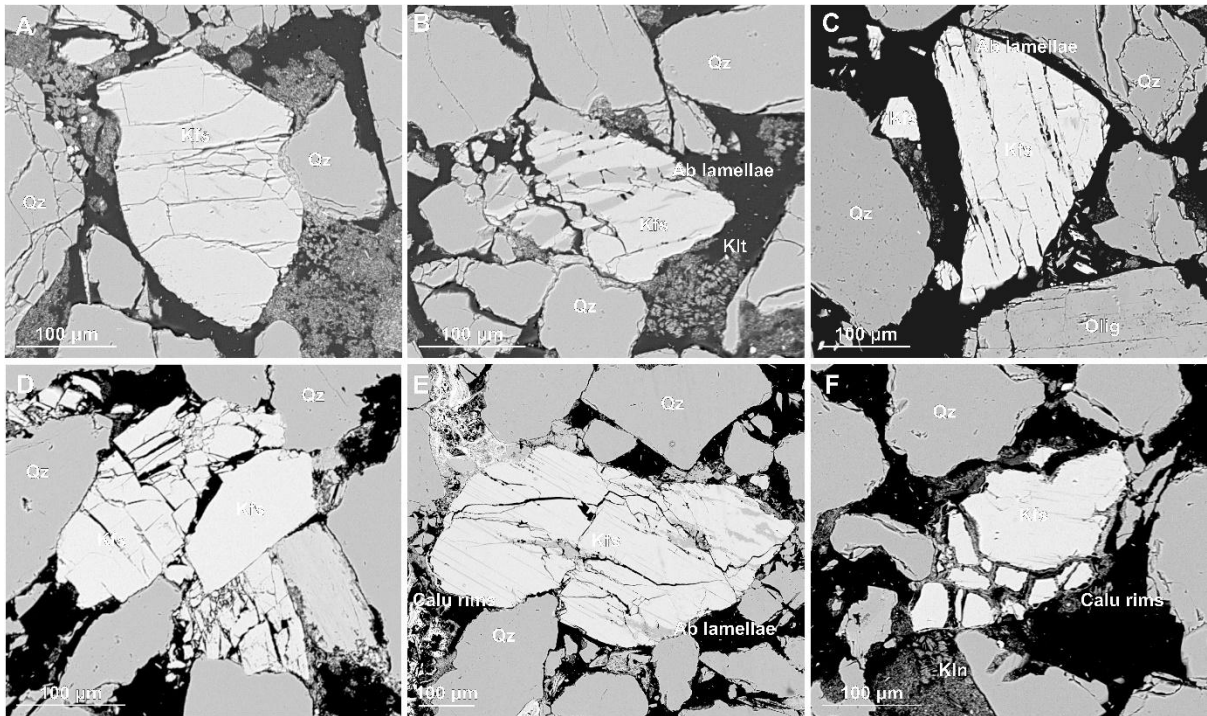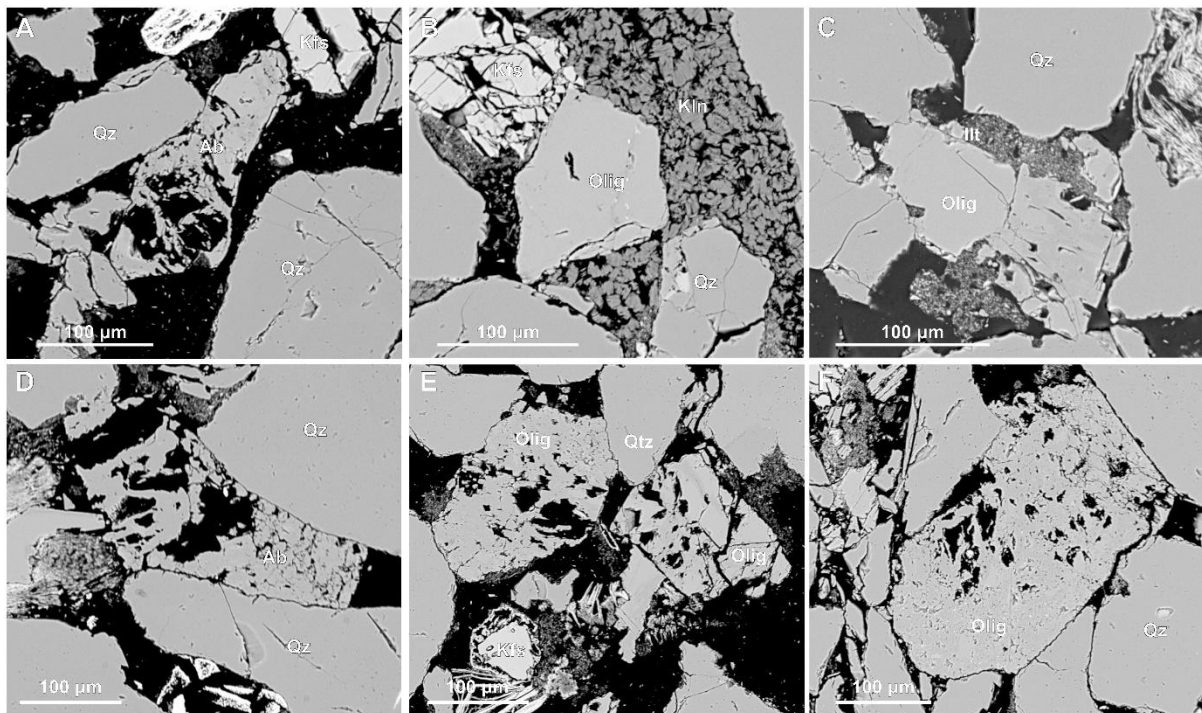

Figure 6. Back scattered electron images showing mechanical fracturing of K-feldspar grains in reaction experiments with H_2O pore fluid at 80°C (a and b), 250°C and 400°C (c and d) and 550°C (e and f). Fractures are generally grain bound with irregular, curvilinear traces and some crystallographic alignment at experiments conducted at higher temperatures (c and e) indicating mechanical weakening. Minimal K-feldspar dissolution and persistent presence of albite lamellae suggest reduced alteration under H_2O compared to CO_2-saturated conditions.

3.2. Alteration of plagioclase

3.2.1. Plagioclase:CO_2 enriched pore fluids

The Captain Sandstone Member contains two types of plagioclase: Na-rich end member albite and intermediate oligoclase (Fig 2). The impact of CO_2 enriched pore fluids on oligoclase and albite, is markedly different to each other. At 80°C (reservoir temperature) albite grains remain coherent/intact with their original grain boundaries and skeletal textures (Fig 7.a) while oligoclase grains show minor marginal dissolution or 'scalloping' along grain edges (Fig 7.b). At 250°C, oligoclase grains have complex, indented grain boundaries often surrounded by kaolinite and mixed-element fine clays (Fig. 7.b, c). Some grains show evidence of intergranular pore development or surface etching, though intergranular microfracturing is limited or absent. At higher temperatures (>400°C), intergranular porosity in oligoclase increases due to grain dissolution (Fig. 7.e, f). Albite grains also show significant intergranular

14

371 porosity, though this appears consistent with the skeletal textures observed in pre-experiment

372 sandstones (Fig. 7.d).

373
374 **Figure 7. Back scattered electron (BSE) images showing plagioclase grains post reaction experiment**
375 **condition with CO_2 enriched fluids. Images show no alteration of albite grains at 80°C or 550°C (a and d)**
376 **while oligoclase grains appear partially dissolved on the grain boundaries at 250°C and 400°C (c) and**
377 **etching and intergranular porosity at 550°C (e and f).**

378 Combined BSE and EDS images or oligoclase grains reacted at 400°C show leaching of Ca+

379 from grain edges leaving an original Na-Ca rich grain centre, a ~20-30 µm thick Na rich albitic

380 grain edge plus 2-5 µm calcium aluminosilicate rims similar to features observed on K-feldspar

381 grains but without the void space between the dissolving host grain and secondary precipitate

382 (Fig 8). In contrast, albite shows minimal evidence of chemical interaction with CO_2-enriched

383 fluids at any temperature (Fig. 7.a, d).
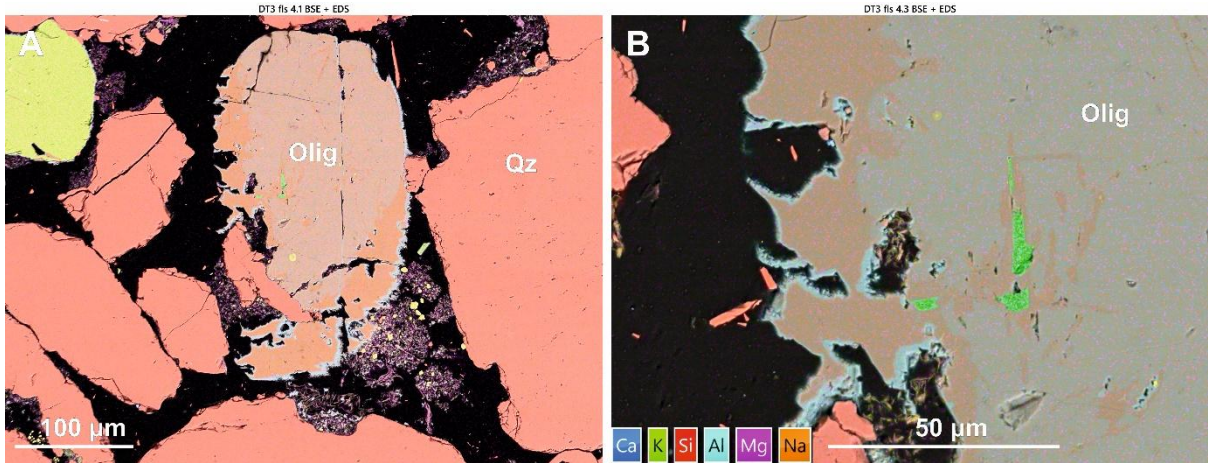
384
385 **Figure 8. Back scattered electron (BSE) images with overlain EDS map showing grain boundary dissolution**
386 **of oligoclase grains reacted with CO_2 fluids at 400°C.**

3.2.2. *Plagioclase:H_2O pore fluids*

388 Experiments run with H_2O pore fluids show no obvious chemical alteration of albite or
389 oligoclase at experiments conducted at 400°C and below, but in these samples the oligoclase
390 grains do show more intergranular fractures with many grains fractured along cleavage planes
391 (Fig 9.a). At higher temperatures (550°C) some oligoclase grains show chemical dissolution
392 and 'scalloping' of the grain boundary (Supp. Mat, Fig 12) with few grains exhibit a thick,
393 porous texture calcite overgrowths apparently tracking the original grain boundary as this
394 boundary abuts the contact with quartz grains (Fig 9.e and f). In this sample calcite cements
395 are still present as singular, isolated patches of cement (Fig 10.c and Supp. Mat, Fig 13).


396
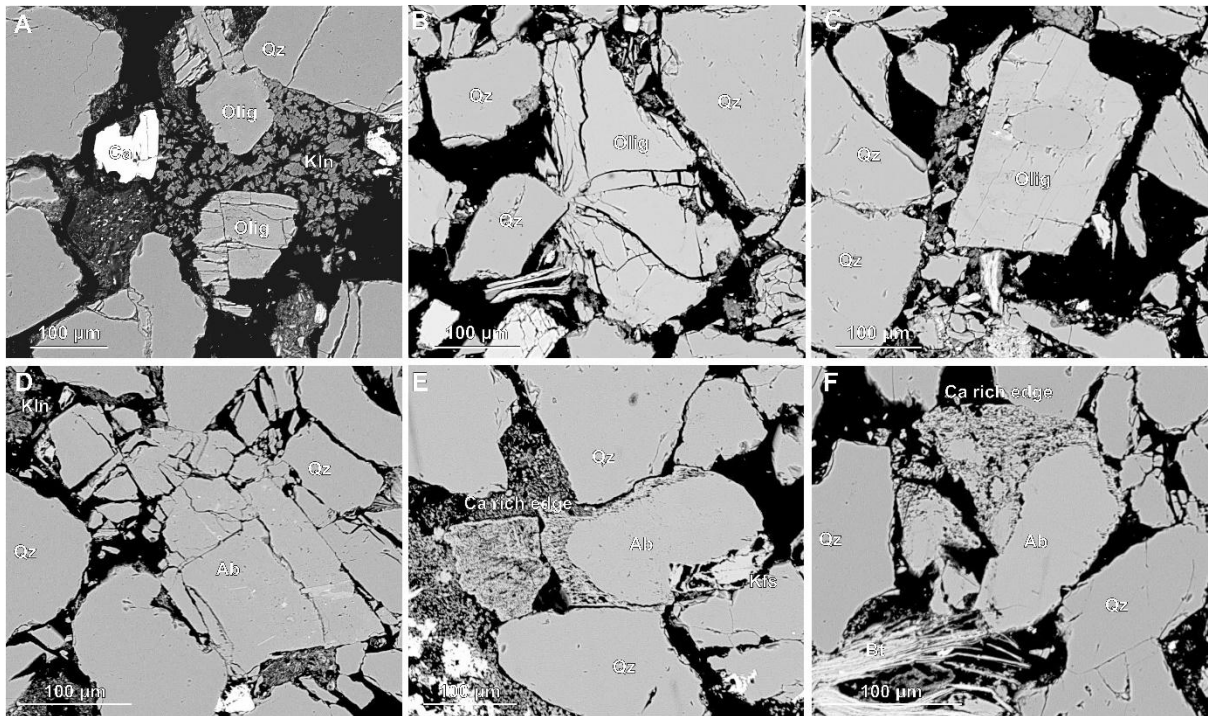
16

397 **Figure 9. Backscattered electron (BSE) images of plagioclase feldspar grains (including both oligoclase and**
398 **albite) following reaction with H_2O pore fluid. Images from 80°C and 250°C experiments (a–c) show**
399 **enhanced mechanical fracturing with minimal evidence of chemical alteration. Albite reacted at 550°C (d)**
400 **also displays fracturing without signs of chemical dissolution. In contrast oligoclase grains reacted at 550°C**
401 **appear partially dissolved, with sodium leached from the grains, resulting in a calcite rich grain boundary**
402 **presenting with a porous 'mesh' texture (e and f).**

403 *3.3. Dissolution of calcite grains and cement with CO_2 enriched water and H_2O pore fluids*

404 Pre experiment samples recorded XRD analysis recorded around 1% calcite which occurred as

405 both grains and cement (Supp. Mat, Fig 4).   Following the experiments, calcite was nearly

406 entirely removed in the CO_2 experiment samples, whereas it remained visible in post H_2O

407 experiment samples (even at temperatures up to 550 °C) as grains and patches of cement

408 (Figure 10).
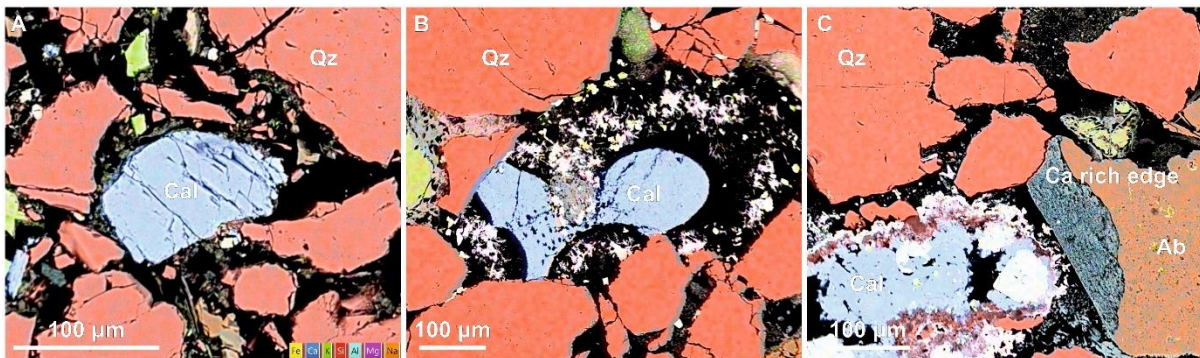
409
410 **Figure 10. Back scattered electron images of calcite grains and calcite cement in post H_2O experiment**
411 **samples reacted at 250°C (a), 400°C (b), 550°C (c).**
412
413 *3.4. Quantitative microstructural and mineralogical alteration*

414 Image analysis was performed to quantify mineral alteration in both CO_2 and H_2O experiment

415 samples. Specifically, changes in the 2D percentage of pore area and the key reactive minerals

416 (K-feldspar, plagioclase, and calcite) were measured. To account for heterogeneity and spatial

417 distribution, the percentage area of each mineral was quantified from multiple subsections of

418 each thin section (between six and twelve 3x3 mm images per sample) following methodology

419 used in Hall et al (2015). The results are presented using box-and-whisker plots to illustrate the

420 data spread and account for heterogeneity (Fig 11). Two pre-experiment samples, 'Dt' and

421 'Dm', were analysed, each with slightly different pre experiment bulk rock compositions (see

422 Supp. Mat, Table 2). Core plugs from the Dm sample were primarily used in H_2O experiments,

423 while Dt sample core plugs were used in CO_2 experiments.

424 Image analysis revealed minimal changes in 2D pore area between pre-experiment samples,

425 which averaged 29% and 32% pore area and post-experiment reacted with H_2O and CO_2 at

426 80°C and 250°C, which averaged 30% and 32%) (Fig 11.a). However, this decreased to 26%

17

427 pore area in samples reacted with H_2O and CO_2 at 400°C and with H_2O 550°C, possibly due to

428 enhanced grain packing and pressure solution observed in images (Fig 9.e and Supp. Mat, Fig

429 11) and secondary mineral precipitation, while samples exposed to CO_2 at 550°C maintained

430 pore areas over 30% (Fig. 4.a). This difference is likely due to additional secondary porosity

431 produced by K-feldspar and calcite cement and grain dissolution (Supp. Mat, Fig 8) as pressure

432 solution and mineral precipitation are also observed in these samples (Fig 7.f and Supp. Mat,

433 Fig 7).

434 Boxplots show the percentage of reactive grains (K-feldspar, plagioclase, and calcite)

435 expressed as their proportion relative to the total number of mineral grains visible in each image

436 (Fig 11.b – d). The average proportion of K-feldspar grains decreased by nearly half in all

437 samples exposed to H_2O and CO_2, with a more significant reduction observed in post CO_2

438 experiment samples (Fig 11.b). These CO_2 reacted samples also exhibited a more

439 heterogeneous distribution of K-feldspar, as indicated by the wider interquartile ranges on the

440 grey CO_2 box-and-whisker plots compared to the blue H_2O boxes, suggesting variable

441 dissolution across the sample (Fig. 11.b). Due to limitations in image thresholding, albite and

442 oligoclase were grouped together under the category of 'all plagioclase'. In samples reacted

443 with CO_2, the proportion of plagioclase decreased by approximately 25%, indicating some

444 dissolution. In contrast, H_2O-reacted samples show little change in plagioclase area (Fig. 11c).

445 XRD analysis determined ~1% calcite in the pre-experiment samples (Supp. Mat, Table 1),

446 observed in thin sections as carbonate clasts, bioclasts, and carbonate cement patches (Supp.

447 Mat, Fig. 4). Quantitative image analysis showed low area fractions of calcite across many pre-

448 and post-experiment images (0–0.9%). Pre-experiment samples had median calcite area

449 fractions of 0.2% and 0.4%, whereas post-experiment samples generally showed lower median

450 values. In CO_2-reacted samples, calcite abundance decreased by more than half at 80 °C and

451 250 °C, with calcite nearly absent at 400 °C and 550 °C (Fig. 11d). In contrast, H_2O-reacted

452 samples showed only a slight decrease at 80 °C, with calcite contents remaining largely

453 unchanged at higher temperatures.
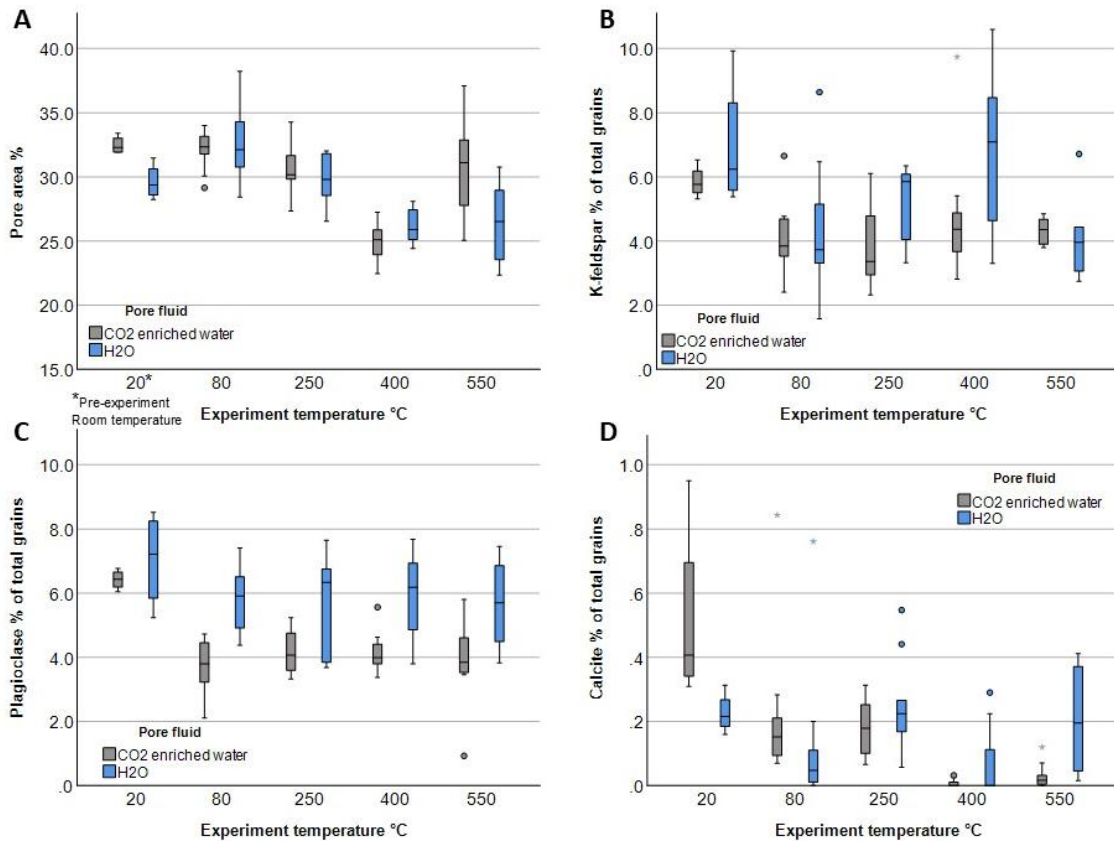
Figure 11. Box and whisker plots d in pore area and reactive mineral content in Captain Sandstone samples before and after reaction, experiments, based on thresholded EDS images. Two pre-reaction samples, 'Dt' and 'Dm', with slightly different bulk compositions were used: Dm cores (H_2O experiments) and Dt cores (CO_2 experiments), shown in grey and blue respectively. Box plots display data spread, including median, interquartile range (IQR), and outliers.

4. Discussion

4.1. Experimental reaction mechanisms and microstructural evolution

Microstructural analysis of reacted samples reveals a complex interplay of feldspar dissolution and secondary mineral precipitation in the presence of H_2O and CO_2-enriched pore fluids. These reactions are driven by deformation mechanisms such as diffusive mass transfer, including pressure solution, microfracturing, which generates fresh surfaces and increases reactivity, ion exchange and hydrolysis. Key contrasts between H_2O and CO_2 fluid experiments samples include: 1) early incongruent dissolution of K-feldspar in CO_2 experiments conducted at 80 °C, as CO_2-enriched fluids, weakened grains and promoted microfracturing; 2) extensive congruent dissolution K-feldspar in higher temperature >250°C experiments with CO_2, which resulted in grain size reduction, creation of secondary pores and increase in pore area; 3) near-

19

471 complete dissolution of calcite grains and cements in CO_2 experiments, compared to partial

472 dissolution with H_2O; and 4) partial dissolution and incongruent leaching of calcium from

473 oligoclase grains from 80 °C with CO_2, resulting in grain area reduction that was not observed

474 in H_2O experiments, (Figure 11). Reactions, deformation mechanisms observed in experiments

475 are summarised in Table 2 and key mineral phases present in the Cretaceous Captain sandstone

476 before, during and after experiments are highlighted in Figure 12.

4.1.1. Feldspar deformation and reaction textures

478 Our results show that at reservoir temperatures CO_2 enriched fluids created a chemically

479 reactive environment that promoted compositionally preferential, incongruent dissolution of

480 K-feldspar and oligoclase. In K-feldspar this produced parallel porous 'seams' that developed

481 on the edge of grains, possibly exploiting cleavage planes (Fig 5.a). These features were absent

482 in higher temperature experiments, possibly because 1) they represented early-stage dissolution

483 textures that were overprinted by later grain dissolution or 2) experiments at higher

484 temperatures (above 250°C) produced a shift in the dominant reaction mechanism from ion

485 exchange reactions (i.e. early incongruent release of K^+, Na^+, and Ca^{2+}) to hydrolysis-driven

486 dissolution (i.e. congruent breakdown of the Si-O framework). Similar temperature-dependent

487 dissolution styles have been observed in previous feldspar reaction experiments on microcline

488 (Fung et al., 1980), albite (Chen et al., 2000), and labradorite (Carroll and Knauss, 2005).

489 K-feldspars with incongruent dissolution textures produced at lower reservoir temperatures

490 appeared to be mechanically weaker and more susceptible to the effects of grain-to-grain

491 stresses under confining pressure, which led to microfracturing and crushing between the more

492 resistant quartz grains (Fig. 4; Supp. Mat. Figs. 5–7). In turn, these 'fresh' microfractures and

493 fragmented grains created more reactive surfaces, which drove further dissolution in a positive

494 feedback loop of 'incongruent dissolution, stress-induced microfracture, and enhanced grain

495 reactivity'. This process likely accelerated the significant K-feldspar comminution and

496 dissolution textures observed after higher temperature experiments.

497 In plagioclase, interaction with CO_2-enriched fluid had no apparent effect on albite grains but

498 oligoclase showed partial dissolution, evident as wavy grain boundaries and localised

499 compositional zoning (Fig 8). EDS analysis indicated that this texture was formed by

500 incongruent dissolution, with calcium being selectively leached from the edge of grains leaving

501 a sodium rich outer zone around an intact Ca-Na rich grain centre (Fig 8). A thin Ca-rich rim

502 at the grain edge was also observed. While grain weakening evidenced by microfracturing was

503 less evident in altered oligoclase grains, pressure solution features (e.g., concave–convex
504 contacts) suggests stress-driven mass transfer played a role in the evolution of these dissolution
505 textures.

4.1.2. Coupled dissolution-precipitation and ion exchange

507 At >400°C in both H_2O and CO_2 experiments, K-feldspar dissolution was coupled with
508 secondary mineral precipitation. This included pore-filling masses, overgrowths and fracture
509 fills of calcic aluminosilicate rims and K-bearing clays associated with dissolving K-feldspar
510 grains (Fig 5.d and Supp Mat., Fig 14). Despite the sharp boundary between the primary K-
511 feldspar and secondary calcic aluminosilicates, optical continuity between secondary phases
512 and host grains indicates epitaxial growth via ion exchange as Ca^{2+} in the pore fluid was
513 substituted for K^+ in K-feldspar. Quantitative surface area analysis showed K-feldspar and
514 calcite as dominant dissolving phases in H_2O and CO_2 experiments (Fig 11). While incongruent
515 dissolution of oligoclase in CO2 experiments contributed additional Ca^{2+} via leaching (Fig. 8).
516 The resulting enrichment likely induced supersaturation, triggering precipitation of calcic
517 aluminosilicates and potassic aluminosilicates (K-clays) (Fig 5).

518 Similar coupled dissolution-precipitation (CDP) reactions in K-feldspar have previously been
519 observed both in nature (Cole et al., 2004, Moore et al, 2005; Baines and Worden; 2004) and
520 experiments (Putnis et al., 2007b; Niedermeier et al, 2009; Norberg et al., 2011; Abart et al.,
521 2012). For example, albitisation of sanidine and orthoclase by Na-Cl fluids via CDP produced
522 sharp reaction interfaces with crystallographically aligned albite overgrowths (Norberg et al.,
523 2011). In another experimental study, the replacement of albite by K-feldspar produced sharply
524 defined reaction fronts while preserving the crystallographic orientation of the host grain
525 (Niedermeier et al., 2009). Additionally, similar to the parallel dissolution seams observed in
526 our study, Niedermeier reported aligned 'tubular nanopores' normal to the replacement interface
527 which they interpreted as pathways for fluid access to the reaction front (Niedermeier et al.,
528 2009). Such nanotube formation appears to be a common feature of reaction fronts in mineral
529 lattices (Harlov et al., 2005; Zeitler et al., (2017).

4.1.3. Anorthitisation of K-feldspar comparison to previous studies

531 In this study, we observed the replacement of K-feldspar by calcic aluminosilicates i.e.
532 'anorthitisation', under experimental conditions (400°C, 70MPa confining pressure).
533 Anorthitisation has been described in natural systems, e.g. the transformation of andesine to

21

534 anorthite in the presence of Ca^{2+}-rich meteoric fluids (Mora et al., 2009) and has been described
535 conceptually in the framework of CDP reactions (Putnis, 2009). Though K-feldspar alteration
536 via direct K^+- Ca^{2+} substitution has not been described previously in geological settings, there
537 are natural examples of K-feldspar alteration involving Ca-bearing fluids. These include high
538 temperature hydrothermal systems where K-feldspar is replaced by Na-Ca plagioclase and
539 myrmekite textures form via K, Na, and Ca exchange (Chakrabarty et al., 2023). And low
540 temperature settings in CO_2-rich basins like Otway and Bravo Dome where fluid acidification
541 drives feldspar dissolution and precipitation of Ca-bearing phases such as dawsonite and calcic
542 zeolites, (Mora et al., 2009; Wigley et al., 2013; Baines and Worden, 2004).

543 While the replacement of K-feldspar by calcic aluminosilicates via ion exchange has not been
544 previously described under controlled laboratory conditions in geoscience, it has been explored
545 and established in materials science. Specifically, anorthitisation via ion exchange is being
546 investigated as a method for extracting potassium from K-feldspar using calcium-bearing fluids
547 as an alternative method for fertiliser production. Although not yet commercially implemented,
548 laboratory studies have shown K^+ leaching from K-feldspar powders at temperatures as low as
549 65°C (Ma et al., 2016; Ciceri et al., 2017), and the formation of calcic aluminosilicate phases,
550 texturally similar to those observed in our experiments, at 160 °C (Liu et al., 2015; Yuanyuan
551 et al., 2020; Haseli et al., 2020; Zhai et al., 2021). These findings suggest that ion exchange via
552 CDP observed in our study may represent a previously unrecognised mechanism for K-feldspar
553 alteration in the presence of CO_2-enriched fluids.

554

555

| Experiment temperature (°C)	K-feldspar		Oligoclase		Albite	
	Chemical alteration	**Mechanical deformation**	**Chemical alteration**	**Mechanical deformation**	**Chemical alteration**	**Mechanical deformation**
80	Localised **incongruent dissolution** producing grain-edge, cleavage-parallel porous seams; preferential release of K^+ ($\pm Na^+$, Ca^{2+})	Stress-assisted **microfracturing** and local grain crushing against quartz, enhanced by chemical weakening	**Incongruent dissolution** around grain boundary with early Ca^{2+} leaching creating scalloped edges	Grains largely intact with no microfracturing	Largely unaltered; skeletal textures preserved	Coherent, no microfracturing
250	Transition toward more **congruent dissolution** along microfractures, increasing reactive surface area	Intergranular **microfracturing** generating fresh reactive surfaces	Continued **incongruent dissolution producing** some intergranualar porosity and indented grain boundaries rimmed by kaolinite and mixed clays	Minor deformation with compaction and minor **microfracturing**	Largely unaltered	Coherent, no microfracturing
400	Coupled dissolution–precipitation (CDP) reaction during K-feldspar dissolution and precipitation of thin (~3 µm) calcic aluminosilicate rims and K-bearing clays via ion exchange (K^+–Ca^{2+})	Sets of through-going, **cross-cutting microfractures** possibly aligned along cleavage and/or chemically altered grain	**Dissolution** increases intergranular porosity by **leaching** of Ca^{2+} from edges leaving 20–30 µm Na-rich boundary and thin 2–5 µm Ca-rich rim	Limited **microfracturing,** fractures less pervasive than K-feldspar	Minimal chemical change	Coherent, skeletal textures maintained
550	Extensive congruent dissolution and grain comminution producing significant secondary porosity. Precipitation of thick (~10 µm) calcic aluminosilicate (anorthitisation) and K-clays	Concave–convex grain contacts with quartz indicating **pressure solution**	Continued **dissolution** and **precipitation** developing albitic rims and enhancing intergranular porosity	Minor **pressure solution** features at grain contacts	Largely unaltered	Coherent, skeletal textures maintained

Table 2. Summary of observed chemical and mechanical alteration and interpreted reactions and deformation mechanisms from experiments reacting CO2 enriched fluids with core plugs of Cretaceous Captain Sandstone 'D sand' from the Acorn CCS field.

23

4.1.4. Source of calcium

In natural systems, Ca^{2+} is typically derived from hydrothermal fluids or CO_2-enriched waters that leach calcium from carbonates, plagioclase, or mafic phases. In our experiments, elevated calcium in the pore fluid resulted from 1) dissolution of calcite grains and cement, prominent in all CO_2 experiments, and to a lesser degree in H_2O experiments >400°C, and 2) partial dissolution of oligoclase, observed only in CO_2 experiments. Incongruent dissolution of plagioclase is well established, for example, a previous experimental study on labradorite showed that calcium release rates exceeded silica release by a factor of three, highlighting strongly incongruent behaviour (Knauss and Wolery, 1988). This likely explains why we observed preferential calcium leaching from oligoclase, producing a Na-rich rim around an intact Na-Ca grain core. The precipitation of secondary calcic aluminosilicate phases may have further contributed to calcium leaching, as the removal of Ca^{2+} from the pore fluid enhanced chemical disequilibrium and promoted continued oligoclase dissolution.

Previous studies on the Captain Sandstone 'D sand' also observed calcite dissolution during CO_2 flow-through experiments at <60 °C (Hangx et al., 2013). However, this study focused on the effect of calcite dissolution on rock mechanical strength and, although they also noted K-feldspar dissolution, did not examine the coupled mechanisms driving geochemical alteration or potential for ion exchange.
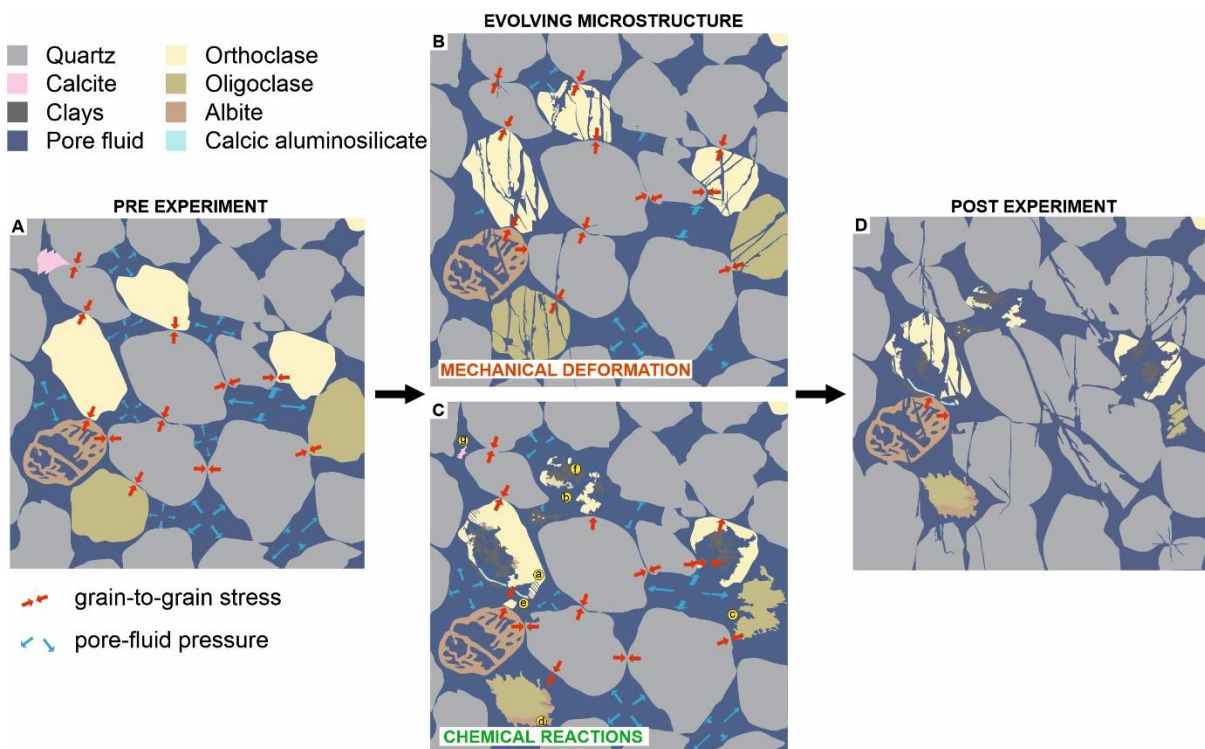
Figure 12. Schematic summary of the coupled mechanical and chemical changes identified from hydrostatic batch experiments using CO₂-enriched pore fluids on the Captain Sandstone ('D sand'). Experiments were conducted at reservoir-relevant confining and pore fluid pressures, generating grain to grain scale stresses at temperatures of 80–550 °C. These conditions promote interacting mechanical and chemical feedbacks that drive the evolution of sandstone microstructure and texture. (A) Pre-experimental sandstone texture with intact K-feldspar (orthoclase), calcic plagioclase (oligoclase), skeletal albite, and minor calcite cement (B) Mechanical deformation preferentially fractures feldspars relative to quartz, creating fresh reactive surfaces and increasing feldspar–fluid contact. (C) Chemical reactions include (a) orthoclase dissolution expressed as parallel cracks penetrating from grain margins to interiors, (b) orthoclase grain dissolution, (c) oligoclase dissolution, (d) albitisation of oligoclase, (e) precipitation of calcic aluminosilicate, (f) precipitation of clay minerals (muscovite–illite), and (g) dissolution of calcite cement. (D) Post-experiment analysis illustrates how coupled deformation–dissolution and new mineral precipitation reshape the microstructure.

4.1.5. Role of stress

Although our experiments were successfully designed to limit mechanical compaction (confirmed by maintenance of pore area in H_2O and CO_2 runs up to 250 °C), features indicative of chemical compaction via pressure solution, such as concave–convex grain contacts, were observed in both H_2O and CO_2 experiments above 400 °C. These suggest localised, stress-assisted dissolution at grain contacts under high temperature aka faster reaction rate experiments. This dissolution likely increased local K^+ concentration, providing micro-zones of supersaturation and promoting precipitation in adjacent lower-stress areas around grain boundaries. Analogous features are seen in natural CO_2 reservoirs like the Supai Sandstone Formation, where dawsonite precipitates are spatially associated with corroded K-feldspar and in the Triassic Chaunoy Formation, which associates feldspar dissolution textures with carbonate and zeolite formation (Moore et al., 2005; Baines and Worden, 2004 respectively).

4.2. Comparison to previous studies on CO₂:sandstone interaction

The enhanced dissolution of K-feldspar and calcite in CO_2-enriched fluids observed in our study aligns with previous experimental studies. For instance, a three-month CO_2 flow-through experiment at 140 °C resulted in K-feldspar dissolution, grain size reduction, and secondary porosity, leading to a 20% increase in porosity and increased permeability (Hall et al., 2015). Although no secondary precipitation occurred due to constant undersaturation, deformation textures e.g. altered feldspars and secondary porosity, closely resemble observations from our experiments. In addition to the dissolution of calcite cement noted in the Hangx study described above, carbonate mineral dissolution in sandstones reacted with CO_2-enriched fluids is

613   experimentally well established. Several studies have shown increased calcium concentrations

614   in pore fluids following saturation of sandstone samples with CO_2 -enriched brines, many

615   accompanied by a corresponding permeability increase (Ross et al., 1982; Sayegh et al., 1990;

616   Hall, 2015; Foroutan, 2021). Precipitation of secondary phases was apparently not a limiting

617   factor for K-feldspar dissolution in our experiments, contrasting with the experimental results

618   of Lu et al, (2013), possibly due to fracture-induced increases in feldspar-fluid surface area.

619   Studies on feldspar alteration in geological CO_2-injection projects and natural CO_2 reservoirs

620   also support our findings. In a study on the microstructural impact of CO_2 on sandstone in an

621   engineered subsurface setting, the microstructure of pre- and post-core CO_2 flood sandstones

622   from the Pembina Cardium CO_2 Monitoring Project in Canada showed partial dissolution of

623   K-feldspar grains after two years of CO_2 injection (Nightingale et al., 2009). And as previously

624   noted, natural CO_2 reservoirs such as Bravo Dome also show feldspar alteration and secondary

625   mineral formation linked to long-term CO_2 exposure (Wigley et al., 2012). These findings

626   confirm that feldspar alteration and associated secondary porosity development can occur over

627   relatively short timescales in the subsurface and are comparable in character to the features we

628   have observed in our higher-temperature experimental system.

4.3. Implications for CCS reservoirs

630   Our findings have several *direct* implications for geological storage of CO_2. Firstly, they

631   demonstrate that K-feldspar and oligoclase in CO_2-enriched fluids at reservoir-relevant

632   conditions can undergo rapid alteration including grain microcracking, dissolution and the

633   development of secondary porosity. Second, they show that dissolution of even small amounts

634   (e.g. 1%) of calcite grains and cement or leaching of calcium from plagioclase can elevate Ca^{2+}

635   concentrations in the pore fluid and, depending on local fluid composition and saturation states,

636   promote ion exchange with K-feldspar and drive the precipitation of calcic aluminosilicates

637   and K-bearing clays. Third, the presence of pressure solution textures suggests that local stress

638   concentrations create grain-scale chemical disequilibria, enhancing feldspar dissolution and

639   promoting localised mineral precipitation, processes that are often overlooked in geochemical

640   models of CCS systems.

641   These microstructural alterations have important implications for reservoir integrity and CCS

642   project performance. Fracturing and dissolution of framework feldspars (~16 % of the D Sand)

643   could reduce compressive strength, alter elastic properties, and modify porosity. These

644   properties are key parameters in both geomechanical and fluid flow models and could alter the

predicted reservoir behaviour. Such changes would be especially critical near structural features like faults, where shifts in strength or porosity may alter fault stability during fluid injection/depletion. While the relatively unfaulted Acorn CCS site may be less susceptible to fault reactivation, microstructural changes such as feldspar fracturing and dissolution could still lead to mechanical compaction and reservoir fracturing. The impact of this may affect the ability to flow CO_2 fluids into the reservoir, i.e. productivity. However, in some cases, such as the Ekofisk field, reservoir collapse and compaction have paradoxically enhanced permeability and improved production (Teufel, 1996).

Secondary mineral precipitation, such as K-bearing illite, could reduce permeability and hinder CO_2 injection/migration, but feldspar dissolution, especially of Ca-bearing phases like oligoclase may enhance long-term CO_2 sequestration by releasing Ca^{2+}. that can become incorporated into secondary phases, possibly even locking in carbon. However, if Ca^{2+} instead bonds with dissolving K-feldspar, it may reduce carbonate formation and limit carbon trapping through mineralisation. Dawsonite did not form in our experiments, likely due to the low Na and Cl content of our fluids. In natural CCS settings, brine compositions with higher Na concentrations could promote dawsonite or other Na-bearing phase formation via K-feldspar replacement. Instead, we observed formation of a calcic aluminosilicate, although we cannot confirm whether it contained carbon, as our carbon-coated thin sections compromised EDS detection.

4.4. Experimental limitations

While our findings offer empirical evidence for feldspar reactivity in CO_2-enriched fluids, several limitations are acknowledged. Most notably, the elevated temperatures used in some experiments accelerated reaction kinetics beyond those typical of natural systems. However, the occurrence of similar dissolution reactions, albeit to a lesser extent, at reservoir temperatures supports the relevance of our results to CCS reservoir and a comparison to reaction rates on a geological timescale has been calculated (Supp Mat). Post-quench precipitation of secondary phases cannot be ruled out, although the presence of well-crystallised calcic aluminosilicate in optical continuity with host grains strongly suggest that these minerals formed in situ during the experiments. This interpretation is consistent with previous work which noted similar limitations and applied the same criteria to distinguish in-experiment from post experiment precipitation (Rosenqvist et al., 2001).

For this study, we employed batch reactor experiments because they allow direct comparison with the geochemical models used in the Acorn CCS Project (Shell, 2015. Batch systems are optimal for studying both dissolution and precipitation processes as they more closely mimic the generally static fluid conditions in subsurface reservoirs than flow through setups. However, batch reactors do not simulate the effects of fluid flow, which in a CCS reservoir would significantly influence reaction kinetics as the dissolved phases would be transported, both reducing supersaturation and making for a dynamic ongoing pore fluid chemistry. As previous CO_2:sandstone flow-through experiments have shown, undersaturation of the fluid suppresses precipitation but enhances feldspar dissolution (Hall et al, 2015). For understanding the interplay between reaction rate and transport in dynamic subsurface environments like CCS reservoirs, both experimental styles are important. Another limitation is the use of tap water rather than brine. Although selected to avoid the overly reactive behaviour of deionised water, our fluid lacks the high Na^+ and Cl^- content typical of formation waters, which may influence both dissolution and secondary mineral precipitation. Future work should incorporate brine compositions and use flow-through systems under triaxial stress to better simulate reservoir conditions.

Despite these limitations, our results provide some of the first experimental evidence for CO_2 fluid induced K-feldspar alteration under controlled conditions relevant to CCS subsurface settings. This supports the idea that K^+–Ca^{2+} exchange can occur via coupled dissolution–precipitation mechanisms, with implications for feldspar reactivity, reservoir evolution, and long-term mineral trapping in CCS scenarios.

5. Summary

This study offers new insights into mineral transformations and grain-scale deformation in a planned CCS reservoir - processes that have been previously recognised in CO_2:sandstone studies but never systematically investigated. This study also provides the first geological evidence that Ca^{2+} released from experimental dissolution of detrital feldspar grains in a sandstone (i.e. not freshly ground-up powder) can drive in-situ K^+ - Ca^{2+} ion exchange in K-feldspar under realistic subsurface conditions.

Consistent with our hypothesis, experimental results showed that:

1) K-feldspar is more reactive than expected when exposed to disequilibrium fluids (both H_2O and CO_2) under subsurface hydrostatic stresses at temperature; and

707 2) in comparison to H_2O, CO_2-enriched fluids significantly altered solubility of both
708 plagioclase and K-feldspar and produced distinct microstructural changes even during short (6-
709 day) experiments.

710 At reservoir temperatures (80 °C), CO_2-enriched fluids induced incongruent dissolution and
711 deformation of K-feldspar and dissolution of detrital calcite via ion exchange underscoring the
712 relevance of these transformations to CCS settings. At higher temperatures, where reaction
713 kinetics were accelerated, both H_2O and CO_2 fluids promoted dissolution of reactive minerals
714 - K-feldspar, oligoclase, and calcite - leading to the precipitation of secondary aluminosilicate
715 and clay phases. We propose that these transformations reflect a coupled dissolution–
716 precipitation mechanism, where Ca^{2+} released from calcite and oligoclase dissolution activates
717 and sustains K-feldspar alteration and subsequent dissolution. Crucially, the formation of
718 epitaxial Ca-bearing overgrowths on K-feldspar grains provides clear experimental evidence
719 for K^+ - Ca^{2+} ion exchange. While this anorthitisation of K-feldspar has been engineered in
720 materials science studies using Ca-rich fluids, this study is the first to demonstrate the reaction
721 occurring *in situ*—i.e., within intact rock, under subsurface stress using weakly CO_2-enriched
722 fluids.

723 As discussed, previous experimental and natural studies show that feldspar alteration can
724 involve coupled dissolution, ion exchange, and secondary mineral formation. Our findings
725 build on this by demonstrating more varied modes of feldspar transformation with CO_2-
726 enriched and calcium bearing fluids. While consistent with earlier CO_2- sandstone work, this
727 study uniquely combines microstructural and geochemical changes created under known
728 conditions to map possible reaction pathways and quantify the impact on mineral texture and
729 microstructure. These processes, often difficult to capture in reactive transport models, could
730 significantly affect reservoir properties like pore volume, fluid flow, and geomechanical
731 integrity.

5.1. Outlook on remaining challenges

733 Chemical mapping and compositional analyses suggest that feldspar zoning may influence
734 dissolution behaviour, although further investigation is required. The original chemical
735 homogeneity of the feldspars and their provenance appear to be important factors controlling
736 reactivity, which could have implications for other arkosic reservoir systems. More broadly,
737 this study raises new questions about the timing and mechanisms of feldspar reactivity in
738 stressed, fluid-saturated environments. It demonstrates the need to reconsider CCS appraisal

739 approaches, which often assess geochemical and geomechanical behaviour separately. Our
740 findings support a more integrated understanding of these processes and have wider relevance
741 for other subsurface applications, including geothermal energy and mineral extraction. Finally,
742 quantifying feldspar dissolution kinetics remains a key challenge due to the formation of
743 secondary clays and interactions with other phases. Future work should focus on simplified,
744 monomineralic synthetic systems with controlled textures and grain sizes to isolate, and thereby
745 better constrain, reaction rates.

746 **Author contribution**: Design of this project and acquisition of funding were carried out by
747 Natalie Farrell, Michael Flowerdew, and Kevin Taylor. Natalie Farrell designed the
748 experiments and prepared samples, and PDRA's Lining Yang and Nico Bigaroni carried them
749 out. Lee Paul provided technical support i.e. tooling, fixing the rig pump. Michael Flowerdew
750 and Lewis Hughes collected SEM BSE and EDS images. Natalie Farrell, Michael Flowerdew,
751 Chris Mark and Michael Pointon conducted analysis of microstructural and geochemical data.
752 Buhari Ardo and Kevin Taylor collected XCT data and processed and analysed the images.
753 John Waters carried out XRD analysis. Natalie Farrell prepared the manuscript with
754 contributions from all co-authors.

763 **References**

764 Alcalde, J., Heinemann, N., Mabon, L., Worden, R.H., De Coninck, H., Robertson, H., Maver,
765 M., Ghanbari, S., Swennenhuis, F., Mann, I. & Walker, T., 2019. *Acorn: Developing full-chain*
766 *industrial carbon capture and storage in a resource- and infrastructure-rich hydrocarbon*
767 *province*. Journal of Cleaner Production, 233, pp. 963–971.

768 Baines, S.J. and Worden, R.H., 2004. The long-term fate of CO2 in the subsurface: natural
769 analogues for CO2 storage.

770 Benson, S.M. and Cole, D.R., 2008. CO2 sequestration in deep sedimentary
771 formations. *Elements*, *4*(5), pp.325-331.

772 Bertier, P., Swennen, R., Laenen, B., Lagrou, D. and Dreesen, R., 2006. Experimental
773 identification of CO2–water–rock interactions caused by sequestration of CO2 in Westphalian
774 and Buntsandstein sandstones of the Campine Basin (NE-Belgium). *Journal of geochemical*
775 *exploration*, *89*(1-3), pp.10-14.

776 Blum, A.E., Stilling. L. 1995. Feldspar dissolution kinetics. *Chemical weathering rates of*
777 *silicate minerals*, pp.291-351. Brantley, S.L., Kubicki, J.D. and White, A.F. eds., 2008.
778 Kinetics of water-rock interaction.

779 Carroll, S.A. and Knauss, K.G., 2005. Dependence of labradorite dissolution kinetics on CO2
780 (aq), Al (aq), and temperature. *Chemical Geology*, *217*(3-4), pp.213-225.

781 Putnis, C.V., Geisler, T., Schmid-Beurmann, P., Stephan, T. and Giampaolo, C., 2007. An
782 experimental study of the replacement of leucite by analcime. *American Mineralogist*, *92*(1),
783 pp.19-26.

784 Chakrabarty, A., Mukherjee, S., Karmakar, S., Sanyal, S. and Sengupta, P., 2023. Petrogenesis
785 and in situ U-Pb zircon dates of a suite of granitoid in the northern part of the Central Indian
786 tectonic Zone: Implications for prolonged arc magmatism during the formation of the
787 Columbia supercontinent. *Precambrian Research*, *387*, p.106990.

788 Chen, Y., Brantley, S.L. and Ilton, E.S., 2000. X-ray photoelectron spectroscopic measurement
789 of the temperature dependence of leaching of cations from the albite surface. *Chemical*
790 *Geology*, *163*(1-4), pp.115-128.

791 Ciceri, D., de Oliveira, M. and Allanore, A., 2017. Potassium fertilizer via hydrothermal
792 alteration of K-feldspar ore. *Green Chemistry*, *19*(21), pp.5187-5202.

793 Cole, D.R., Larson, P.B., Riciputi, L.R. and Mora, C.I., 2004. Oxygen isotope zoning profiles
794 in hydrothermally altered feldspars: Estimating the duration of water-rock
795 interaction. *Geology*, *32*(1), pp.29-32.

796 Collettini, C., Tesei, T., Scuderi, M.M., Carpenter, B.M. and Viti, C., 2019. Beyond Byerlee
797 friction, weak faults and implications for slip behavior. *Earth and Planetary Science*
798 *Letters*, *519*, pp.245-263.

799   Correns, C.W., 1961, February. Experiments on the decomposition of silicates and discussion
800   of chemical weathering. In *Clays and Clay Minerals (National Conference on Clays and Clay*
801   *Minerals)* (Vol. 10, pp. 443-459). Cambridge University Press & Assessment.

802   Dove, P.M. and Crerar, D.A., 1990. Kinetics of quartz dissolution in electrolyte solutions using
803   a hydrothermal mixed flow reactor. *Geochimica et cosmochimica acta*, *54*(4), pp.955-969.

804   Durst, P. and Vuataz, F.D., 2000, June. Fluid-rock interactions in hot dry rock reservoirs. A
805   review of the HDR sites and detailed investigations of the Soultz-sous-Forets system.
806   In *Proceedings World Geothermal Congress* (pp. 3677-3682). Kyushu-Tohoku Japan.

807   Farrell, N.J.C. and Healy, D., 2017. Anisotropic pore fabrics in faulted porous
808   sandstones. *Journal of Structural Geology*, *104*, pp.125-141.

809   Farrell, N.J.C., Debenham, N., Wilson, L., Wilson, M.J., Healy, D., King, R.C., Holford, S.P.
810   and Taylor, C.W., 2021. The effect of authigenic clays on fault zone permeability. *Journal of*
811   *Geophysical Research: Solid Earth*, *126*(10), p.e2021JB022615.

812   Flowerdew, M.J., Farrell, N., Yang, L., Badenszki, E,. Mark, C,. Ardo, B. and Taylor, K.:
813   Feldspars in CCS reservoirs: overlooked or unimportant?, CCS4G Symposium 2024, 17
814   December 2024, https://www.ges-gb.org.uk/events/ccs4g-symposium-2024/, 2024.

815   Folk, R.L., Andrews, P.B. and Lewis, D.W., 1970. Detrital sedimentary rock classification and
816   nomenclature for use in New Zealand. *New Zealand journal of geology and geophysics*, *13*(4),
817   pp.937-968.

818   Foroutan, M., Ghazanfari, E. and Amirlatifi, A., 2021. Variation of failure properties, creep
819   response and ultrasonic velocities of sandstone upon injecting CO2-enriched
820   brine. *Geomechanics and Geophysics for Geo-Energy and Geo-Resources*, *7*(2), p.27.

821   Fuchs, S.J., Espinoza, D.N., Lopano, C.L., Akono, A.T. and Werth, C.J., 2019. Geochemical
822   and geomechanical alteration of siliciclastic reservoir rock by supercritical CO2-saturated brine
823   formed during geological carbon sequestration. *International Journal of Greenhouse Gas*
824   *Control*, *88*, pp.251-260.

825   Fung, P.C., Bird, G.W., McIntyre, N.S., Sanipelli, G.G. and Lopata, V.J., 1980. Aspects of
826   feldspar dissolution. *Nuclear technology*, *51*(2), pp.188-196.

827   Glasmann, J.R., 1992. The fate of feldspar in Brent Group reservoirs, North Sea: A regional
828   synthesis of diagenesis in shallow, intermediate, and deep burial environments. *Geological*
829   *Society, London, Special Publications*, *61*(1), pp.329-350.

830   Hall, M.R., Dim, P.E., Bateman, K., Rochelle, C.A. and Rigby, S.P., 2015. Post-CO2 injection
831   alteration of pore network geometry and intrinsic permeability of Permo Triassic sandstone
832   reservoir". Geofluids, 10.1111/gfl. 12146.

833   Hangx, S., Bakker, E., Bertier, P., Nover, G. and Busch, A., 2015. Chemical–mechanical
834   coupling observed for depleted oil reservoirs subjected to long-term CO2-exposure–A case
835   study of the Werkendam natural CO2 analogue field. *Earth and Planetary Science Letters*, *428*,
836   pp.230-242.

837   Harlov, D.E., Wirth, R. and Förster, H.J., 2005. An experimental study of dissolution–
838   repreciptation in fluorapatite: fluid infiltration and the formation of monazite. *Contributions*
839   *to Mineralogy and Petrology*, *150*(3), pp.268-286.

840   Haseli, P., Majewski, P., Christo, F., Raven, M., Klose, S. and Bruno, F., 2020. Experimental
841   kinetic analysis of potassium extraction from ultrapotassic syenite using NaCl–CaCl2 salt
842   mixture. *Acs Omega*, *5*(27), pp.16421-16429.

843   Helgeson, H.C., Murphy, W.M. and Aagaard, P., 1984. Thermodzhuynamic and kinetic
844   constraints on reaction rates among minerals and aqueous solutions. II. Rate constants,
845   effective surface area, and the hydrolysis of feldspar. *Geochimica et Cosmochimica*
846   *Acta*, *48*(12), pp.2405-2432.

847   Hellmann, R., Wirth, R., Daval, D., Barnes, J.P., Penisson, J.M., Tisserand, D., Epicier, T.,
848   Florin, B. and Hervig, R.L., 2012. Unifying natural and laboratory chemical weathering with
849   interfacial dissolution–repreciptation: a study based on the nanometer-scale chemistry of
850   fluid–silicate interfaces. *Chemical Geology*, *294*, pp.203-216.

851   IPCC, 2005. *Special Report on Carbon Dioxide Capture and Storage*. Cambridge:
852   Cambridge University Press, 431 pp.

853   Juanes, R., Spiteri, E.J., Orr Jr, F.M. and Blunt, M.J., 2006. Impact of relative permeability
854   hysteresis on geological CO2 storage. *Water resources research*, *42*(12).

855   Knauss, K.G. and Wolery, T.J., 1986. Dependence of albite dissolution kinetics on pH and time
856   at 25 C and 70 C. *Geochimica et Cosmochimica Acta*, *50*(11), pp.2481-2497.

857   Liu, S.K., Han, C., Liu, J.M. and Li, H., 2015. Hydrothermal decomposition of potassium
858   feldspar under alkaline conditions. *Rsc Advances*, *5*(113), pp.93301-93309.

859   Lu, P., Fu, Q., Seyfried Jr, W. E., Hedges, S. W., Soong, Y., Jones, K., Zhu, C., 2013.
860   Coupled alkali feldspar dissolution and secondary mineral precipitation in batch systems–2:

New experiments with supercritical CO2 and implications for carbon sequestration. Appl. Geochem. 30, 75–90.

Ma, X., Ma, H. and Yang, J., 2016. Sintering preparation and release properties of K2MgSi3O8 slow-release fertilizer using biotite acid-leaching residues as silicon source. *Industrial & Engineering Chemistry Research*, *55*(41), pp.10926-10931.

Moore, J., Adams, M., Allis, R., Lutz, S. and Rauzi, S., 2005. Mineralogical and geochemical consequences of the long-term presence of CO2 in natural reservoirs: an example from the Springerville–St. Johns Field, Arizona, and New Mexico, USA. *Chemical geology*, *217*(3-4), pp.365-385.

Mora, C.I., Riciputi, L.R., Cole, D.R. and Walker, K.D., 2009. High-temperature hydrothermal alteration of the Boehls Butte anorthosite: origin of a bimodal plagioclase assemblage. *Contributions to Mineralogy and Petrology*, *157*(6), pp.781-795.

Neusser, G., Abart, R., Fischer, F.D., Harlov, D. and Norberg, N., 2012. Experimental Na/K exchange between alkali feldspar and an NaCl–KCl salt melt: chemically induced fracturing and element partitioning. *Contributions to Mineralogy and Petrology*, *164*(2), pp.341-358.

Niedermeier, D.R., Putnis, A., Geisler, T., Golla-Schindler, U. and Putnis, C.V., 2009. The mechanism of cation and oxygen isotope exchange in alkali feldspars under hydrothermal conditions. *Contributions to Mineralogy and Petrology*, *157*(1), pp.65-76.

Norberg, N., Neusser, G., Wirth, R. and Harlov, D., 2011. Microstructural evolution during experimental albitization of K-rich alkali feldspar. *Contributions to Mineralogy and Petrology*, *162*(3), pp.531-546.

Pessu, F., Macente, A., Sanni, O. and Piazolo, S., 2025. The importance of whole system considerations for sustainable, long-term CO2 injection and storage: Interplay between infrastructure-related corrosion and reservoir rock chemistry effects on the evolution of the CO2 storage capacity. *International Journal of Greenhouse Gas Control*, *148*, p.104520.

Pinnock, S.J., Clitheroe, A.R.J. and Rose, P.T.S., 2003. The Captain Field, Block 13/22a, UK North Sea.

Putnis, A., 2009. Mineral replacement reactions. *Reviews in mineralogy and geochemistry*, *70*(1), pp.87-124.

Rathnaweera, T.D., Ranjith, P.G., Perera, M.S.A., Haque, A., Lashin, A., Al Arifi, N., Chandrasekharam, D., Yang, S.Q., Xu, T., Wang, S.H. and Yasar, E., 2015. CO2-induced

892 mechanical behaviour of Hawkesbury sandstone in the Gosford basin: An experimental
893 study. *Materials Science and Engineering: A*, *641*, pp.123-137.

894 Ringrose, P., 2020. How to store CO2 underground: Insights from early-mover CCS projects.

895 Rochelle, C.A., Czernichowski-Lauriol, I. and Milodowski, A.E., 2004. The impact of
896 chemical reactions on CO2 storage in geological formations: a brief review.

897 Ross, G.D., Todd, A.C., Tweedie, J.A. and Will, A.G., 1982, April. The dissolution effects of
898 CO2-brine systems on the permeability of UK and North Sea calcareous sandstones. In *SPE*
899 *Improved Oil Recovery Conference?* (pp. SPE-10685). SPE.

900 Rutter, E.H., 1976. A discussion on natural strain and geological structure-the kinetics of rock
901 deformation by pressure solution. *Philosophical Transactions of the Royal Society of London.*
902 *Series A, Mathematical and Physical Sciences*, *283*(1312), pp.203-219.

903 Scholz, C.H., 1972. Static fatigue of quartz. *Journal of Geophysical Research*, *77*(11),
904 pp.2104-2114.

905 Seisenbayev, N., Absalyamova, M., Alibekov, A. and Lee, W., 2023. Reactive transport
906 modeling and sensitivity analysis of CO2–rock–brine interactions at Ebeity Reservoir, West
907 Kazakhstan. *Sustainability*, *15*(19), p.14434.

908 Shell, 2015. 'Peterhead CCS Project: Geochemical Reactivity Report CCS-05-PT-ZR-3323-
909 00001. <u>PVT Modelling Report for CO2 in Goldeneye Project</u>

910 Shogenov, K., Shogenova, A., Vizika-Kavvadias, O. and Nauroy, J.F., 2015. Experimental
911 modeling of CO2-fluid-rock interaction: The evolution of the composition and properties of
912 host rocks in the Baltic Region. *Earth and Space Science*, *2*(7), pp.262-284.

913 Stewart, N. and Marshall, J.D., 2020. The Goldeneye Field, Blocks 14/29a and 20/4b, UK
914 North Sea.

915 Summers, R. and Byerlee, J., 1977, May. A note on the effect of fault gouge composition on
916 the stability of frictional sliding. In *International Journal of Rock Mechanics and Mining*
917 *Sciences & Geomechanics Abstracts* (Vol. 14, No. 3, pp. 155-160). Pergamon.

918 Tullis, J. and Yund, R.A., 1977. Experimental deformation of dry Westerly granite. *Journal of*
919 *geophysical research*, *82*(36), pp.5705-5718.

920   Wigley, M., Dubacq, B., Kampman, N. and Bickle, M., 2013. Controls of sluggish, CO2-
921   promoted, hematite and K-feldspar dissolution kinetics in sandstones. *Earth and Planetary*
922   *Science Letters*, *362*, pp.76-87.

923   Whitney, D.L. and Evans, B.W., 2010. Abbreviations for names of rock-forming
924   minerals. *American mineralogist*, *95*(1), pp.185-187.

925   Wollast, R., 1967. Kinetics of the alteration of K-feldspar in buffered solutions at low
926   temperature. *Geochimica et Cosmochimica Acta*, *31*(4), pp.635-648.

927   Wheeler, J., 1991. A view of texture dynamics. *Terra Nova*, *3*(2), pp.123-136.

928   Whitney, D.L., Evans, B.W., 2010. Abbreviations for names of rock-forming minerals.

929   Amer. Mineral. 95, 185–187.

930   YuanYuan, Z., QingDong, Z., Roland, H., ShanKe, L., JianMing, L. and JingBo, N., 2020.
931   Reaction mechanism during hydrothermal alteration of K-feldspar under alkaline conditions
932   and nanostructures of the produced tobermorite. *Acta Petrologica Sinica*, *36*(9), pp.2834-
933   2844.

934   Zeitler, P.K., Enkelmann, E., Thomas, J.B., Watson, E.B., Ancuta, L.D. and Idleman, B.D.,
935   2017. Solubility and trapping of helium in apatite. *Geochimica et Cosmochimica Acta*, *209*,
936   pp.1-8.

937   Zhai, Y., Hellmann, R., Campos, A., Findling, N., Mayanna, S., Wirth, R., Schreiber, A.,
938   Cabié, M., Zeng, Q., Liu, S. & Liu, J., 2021. Fertilizer derived from alkaline hydrothermal
939   alteration of K-feldspar: micrometer to nanometer-scale investigation. *Applied Geochemistry*,
940   126, p.104828.

941